Versatile Magnetic Mesoporous Carbon Derived Nano-Adsorbent for Synchronized Toxic Metal Removal and Bacterial Disinfection from Water Matrices

Atif Saleem, Jingjie Chen, Meng Liu, Nian Liu, Muhammad Usman, Ke Wang, Muhammad Haris, Yuezhou Zhang, Peng Li

Versatile Magnetic Mesoporous Carbon Derived Nano-adsorbent for Synchronized Toxic Metal Removal and Bacterial Disinfection from Water Matrices

Atif Saleem [1], Jingjie Chen [1], Meng Liu [1], Nian Liu [1], Muhammad Usman [2], Ke Wang [1], Muhammad Haris [3], Yuezhou Zhang [1,4], Peng Li [1*]*

[1] Frontiers Science Center for Flexible Electronics (FSCFE), Shaanxi Institute of Flexible Electronics (SIFE) & Shaanxi Institute of Biomedical Materials and Engineering (SIBME), Northwestern Polytechnical University (NPU), 127 West Youyi Road, Xi'an 710072, P. R. China
[2] École Nationale Supérieure de Chimie de Rennes, CNRS, UMR 6226, 35708 Rennes, France
[3]School of Environmental Science and Engineering, Shaanxi University of Science & Technology, Xi'an 710021, PR China
[4] Ningbo Institute of Northwestern Polytechnical University, Frontiers Science Center for Flexible Electronics (FSCFE), Key laboratory of Flexible Electronics of Zhejiang Province, Ningbo Institute of Northwestern Polytechnical University, 218 Qingyi Road, Ningbo, 315103, China
* Correspondence: iamyzzhang@nwpu.edu.cn (Y. Zhang), iampli@nwpu.edu.cn (P. Li)

Keywords: tailormade mesoporous carbon, nano-adsorbent, adsorption, antimicrobial, disinfection, water treatment

Abstract

Contamination of water resources by toxic metals and opportunistic pathogens remains a serious challenge. The development of nano-adsorbents with desired features to tackle this problem is a continuously evolving field. Here, we report magnetic mesoporous carbon nanospheres grafted by antimicrobial polyhexamethylene biguanidine. Detailed mechanistic investigations revealed that the electrostatic stabilizer modified magnetic nanocore interfaced mesoporous shell can be programmatically regulated to tune the size and related morphological properties. The core-shell nano-adsorbent showed tailorable shell thickness (20~55 nm), high surface area (363.47 $m^2 g^{-1}$), pore volume (0.426 $cm^3 g^{-1}$), radially gradient pores (11.26 nm) and abundant biguanidine functionality. Importantly, the nano-adsorbent has high adsorption capacity for toxic thallium (Tl(I) ions (~559 mg g^{-1}), excellent disinfection against *Staphylococcus aureus* and *Escherichia coli* (>99.99 % at

2 and 2.5 μg mL^{-1}), ultrafast disinfection kinetics rate (>99.99 % within ~4 min) and remarkable regeneration capability when exposed to polluted water matrices. The Tl(I) removal was attributed to surface complexation and physical adsorption owing to open ended mesopores, while disinfection relied on contact of terminal biguanidines with phospholipid head groups of membrane. The significance of this work lies in bringing up effective synchronic water purification technology to combat pathogenic microorganisms and toxic metal.

1. Introduction

The scarcity of drinking water resources and contamination due to growing anthropogenic activities is a major issue with adverse effects on environment and human health. According to a recent survey, more than 1.2 billion people do not have access to clean drinking water and causing approximate 14000 deaths every day.[1] Mixed pollutants including toxic heavy metals and pathogenic microbes in fresh water matrices were highly concerned. Thallium (Tl), a distinct heavy metal possess severe toxicity for human being and environment as compared to mercury, lead, cadmium and copper metals.[2] The bacterial strains involved *Staphylococcus aureus* (*S. aureus*) and *Escherichia coli* (*E. coli*) presence further aggravated the problem with waterborne diseases including, typhoid, dysentery, and hepatitis.[3] Most of traditional water treatment methods for removal of toxic metals including precipitation, catalysis, crystallization, osmosis or adsorption have several limitations related to high energy requirements, longer duration, poor removal rate and higher operational cost etc.[1, 4] Similarly, conventional microbial decontamination approached including UV irradiations, chlorination and ozonation required continuous

chemical treatments, which eventually cause the formation of harmful byproducts and raise health concerns.[5] Hence, it is imperative to develop a synchronic combination of more than one technology to cope with the limitation related to conventional water treatment methods since the mixed environmental pollution was often witnessed.[6] Lately, nano adsorbents established as a useful tools for water purification due to their high surface area, versatile functionalities, lower apparent density and speeded interfacial mass transfer.[7] However, nano adsorbents with dual functions for targeting multiple pollutants and having merits of easy separation have been rarely reported and remain underdeveloped.[8]

The rapid advent of nanotechnology has aroused considerable to develop multi-task specific nano-adsorbent for synchronized adsorption and disinfection.[9] The hierarchal mesoporous nanostructures exhibiting programmable distinctive features promised tremendous applications including adsorption, separation, catalysis, biomedicine, and energy storage.[10] A variety of approaches have been developed to synthesize mesoporous polymer derived carbon nanospheres. Among them, soft templating strategy is mostly favored because of its flexible assembly of precursor and surfactant polymers to yield tailormade architectures with desired morphology and functionality.[11] Furthermore, magnetic nature of nano-adsorbents can facilitate their separation from the aqueous system preventing the risks of secondary contamination and offering opportunities for their reuse. Dopamine (DA) molecule with both catechol and amino groups can self-polymerize into polydopamine (PDA) to form a conformal coating on various surfaces in ambient conditions. In addition, the PDA coating shows great potential in post-modification through hydrogen bonds, electrostatic attraction, chelation, and covalent bonds.[12] Cationic polymers such as polyhexamethylene biguanidine (PHMB) have been widely used as a

disinfectant in medicine and wound care due to biocompatibility and potent bactericidal properties.[13] Post modification of mesoporous PDA shell derived carbon with PHMB can efficiently decontaminate multiple pollutants from drinking water. In this regard, the development of core-shell nano adsorbent having combined merits of magnetic core and stable mesoporous shell, which can provide various organic functional groups for further modification and immobilization active sites can serve the simultaneous adsorption and disinfection purpose in real-time scenario.

To this end, a programable polymerization rate induced interface soft assembly of carbon precursors on citrate capped magnetic nanocore were reported. The synthesis of gradient nano-adsorbent achieved by soft assembly of Pluronic F127 surfactant, 1, 3, 5-trimethylbenzene (TMB) as a mediator, and DA as a nitrogen and carbon source in an ethanol/water mixture system and followed by carbonization in N_2 atmosphere. The DA polymerization rate regulated by tuning NH_4OH concentration during assembly process, to yield desired functional mesoporous structure. The PHMB grafted PHMB~g~MMCN$_{@2.5}$ nano-adsorbent has been deeply investigated for Tl(I) uptake, bacterial inhibition of *Staphylococcus aureus* (*S. aureus*), and *Escherichia coli* (*E. coli*) in simulated deionized and lake water matrices to demonstrate its promising potential in practical applications.

2. Results and Discussion

The marvelous core-shell structure of magnetic mesoporous PDA derived carbon nanosphere (MMCN) decorated with vertical 3D aligned meso-channel pore structure was developed by a robust emulsion-induced interface assembly approach. The magnetic nanocore interfaced assembly of PDA shell occurred by congregation of Pluronic F127 (PEO_{106}-PPO_{70}-PEO_{106}) copolymer surfactant and DA as a carbon source, while 2.5 mL of

NH_4OH enables DA polymerization and promoted the deposition kinetic of PDA (denoted as $MMCN_{@2.5}$). In the reaction system, 1, 3, 5-trimethylbenze TMB was used as a pore swelling agent and resultant nanostructures were carbonized under inert N_2 (Scheme 1). Firstly, the PPO segments of F127 surfactant weakly interact with TMB by van der Waals force and form spherical nano micelles,[14] while PEO segments reach outside in the bulk (Figure S1, Supporting Information). The magnetic nanocore and DA dissolved in ethanol were introduced into the reaction system and tended to form a hydrogen bonding between nanocore and spherical F127 and TMB nano-micelles.[15] Here F127 acted as a bridge between TMB and DA, which reduced the surface energy during the polymerization. The composite micelle of DA, surfactant and TMB began to assemble on the citrate modified magnetic nanocore to lower the interface energy of the reaction system. The DA oxidative polymerization into PDA was induced by NH_4OH and phenolic and hydroxyl groups of PDA interacted with EO segments of F127. As the polymerization process proceeded, composite micelles formed curved interfaces perpendicularly encapsulating magnetic nanocores and formed cylindrical mesoporous building blocks of PDA shell. Afterwards, the removal of F127 by carbonization of PDA skeleton converted it into mesoporous carbon nanospheres. Although the exact structure of PDA remains unclear, it contains abundant phenolic hydroxyls, amines, and quinones, which endow PDA with facile reactivity for further post-functionalization.[12] The plenty of phenolic groups present on the interface of $MMCN_{@2.5}$ were capable to react with amino group of PHMB by Michael-type addition or Schiff base reaction catalyzed by DMAP and DCC in the DMF solvent.[16] Therefore, it is inferred PHMB combines with the negatively charged $MMCN_{@2.5}$ to self-assemble into functionally modified PHMB~g~$MMCN_{@2.5}$ nano-adsorbent.

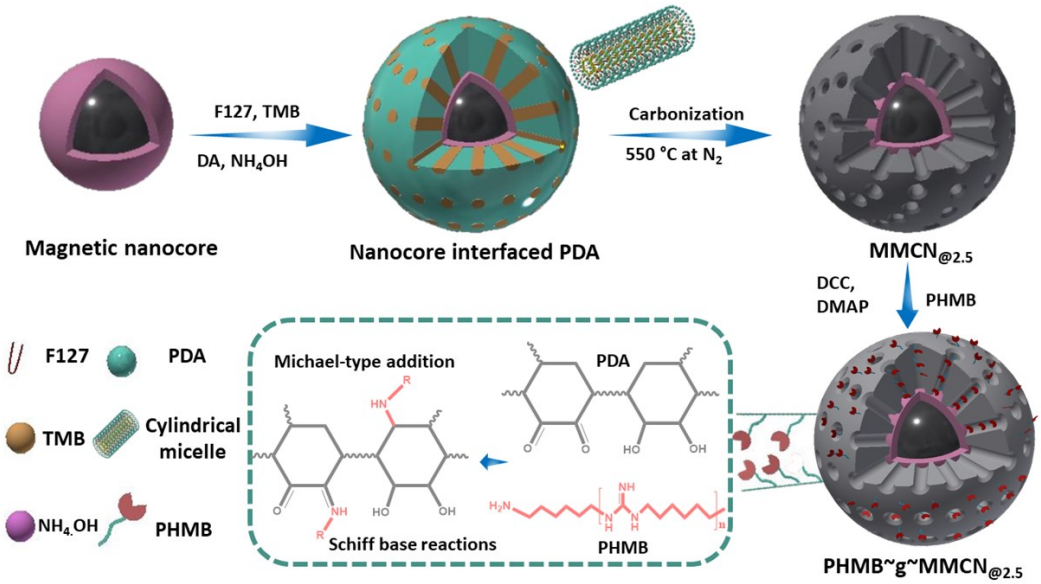

Scheme 1. Schematic diagram of the synthesis process of nano adsorbent.

Primarily, a highly hydrophilic magnetic nanocore exhibiting uniform size of ~225 nm was prepared by a modified hydrothermal method as shown in Figure 1A and S2 in the supporting information. Field emission electron microscope images (Figure 1B) display a core-shell nanostructures of $MMCN_{@2.5}$ in uniform sizes with average diameter of ~260 nm, and gradient open ended mesopores. FESEM image of PHMB~g~$MMCN_{@2.5}$ showed in Figure 1C, represents prominent difference in morphology after the conjugation of antimicrobial polymer on mesoporous carbon shell, which provides visual evidence of successful synthesis of nano-adsorbent. The gradient morphology and uniformly exposed mesopores were further verified by TEM and STEM images (Figure 1D-E). A closer observation of single PHMB~g~$MMCN_{@2.5}$ at a higher TEM resolution reveals that the gradient PDA shell retained its mesoporous framework after graphitization (Figure S3, Supporting Information). Furthermore, energy dispersive X-ray (EDX) elemental mapping observations (Figure 1F-J), displayed that uniform distribution of overlap, Fe, C, O and N

thorough out the surface of nano-adsorbent. Quantitative analysis of the above-mentioned elements present in nano-adsorbent was also confirmed by the EDS spectrum (Figure S4, Supporting Information).

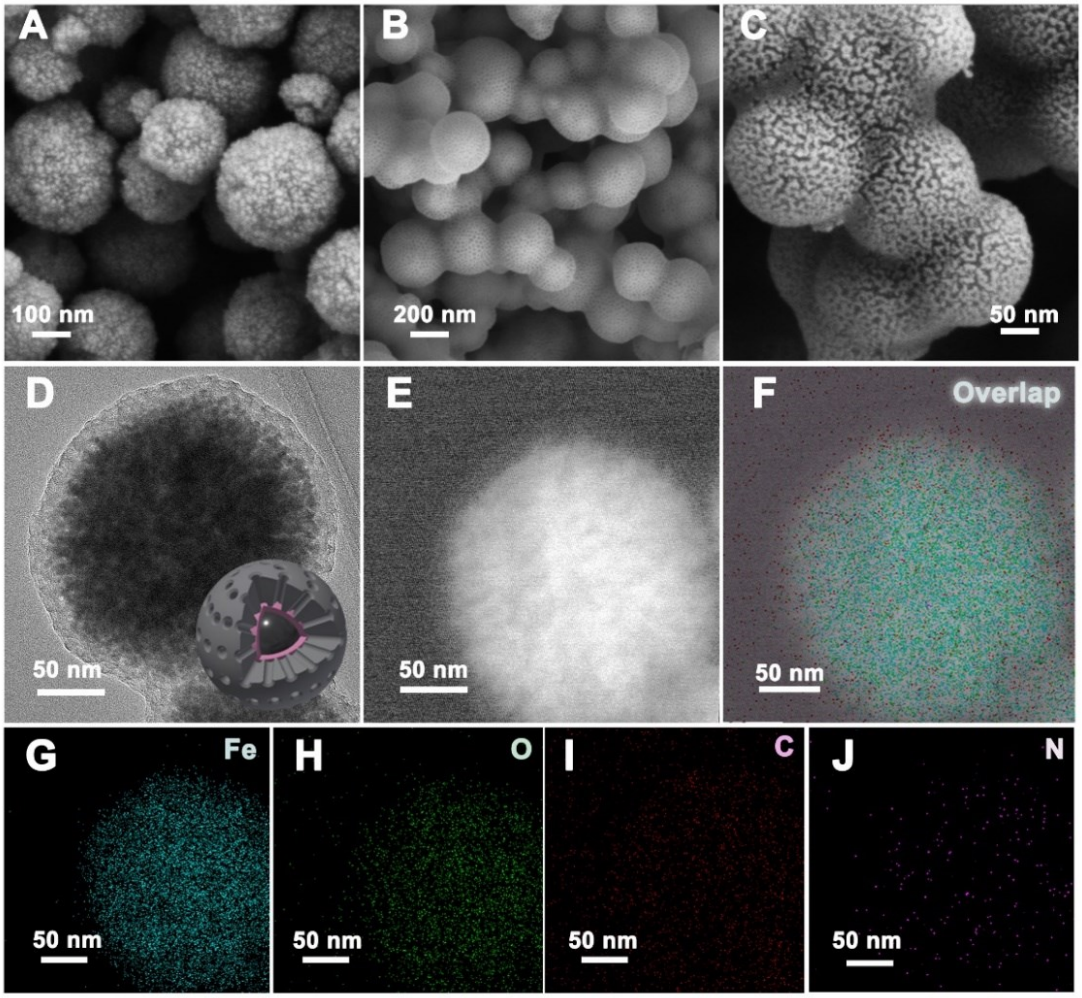

Figure 1. The morphological features observations of PHMB~g~MMCN$_{@2.5}$ nano-adsorbent. A) magnetic nanocore, B) MMCN$_{@2.5}$, C) PHMB~g~MMCN$_{@2.5}$, D) TEM image and inset show 3D framework model of PHMB~g~MMCN$_{@2.5}$, E) STEM observation, F-J) EDX elemental mapping of overlap, Fe, O, C, and N respectively.

Nitrogen adsorption and desorption analysis of PHMB~g~MMCN$_{@2.5}$ showed typical type-IV peaks with a unique capillary condensations step at relatively high pressures of $0.7 < P/P_0 < 1.0$ (Figure 2A), indicated a larger mesopore architecture.[17] The hysteresis loop

exhibited a narrow range, which represents the uniform morphology of mesopores.[18] Pore size distribution was calculated by non-local density functional theory (NLDFT) of adsorption with the mean pore diameter of 11.26 nm, which were near identical to the pore size estimated by TEM observations (Figure S3, Supporting Information). The as calculated surface area, and pore volume was 363.47 m^2g^{-1}, and 0.426 cm^3g^{-1} respectively. The successful interface engineering of $MMCN_{@2.5}$ with bactericidal polymer PHMB were verified by intensive characterization results.

Fourier transform infrared (FTIR) spectroscopy of $MMCN_{@2.5}$ and PHMB~g~$MMCN_{@2.5}$ were examined (Figure 2B) which revealed fingerprint PDA aromatic rings at 1550 to 1620 cm^{-1} in both spectra.[19] The new peaks at 2331 cm^{-1} and 2361 cm^{-1} could be assigned to the stretching vibrations of conjugated PHMB terminal cyano group (−C≡N).[20] Surface charge density of carboxylated magnetic nanocore, $MMCN_{@2.5}$ and cationic polymer conjugated PHMB~g~$MMCN_{@2.5}$ were examined (Figure 2C). The negative potential of magnetic nanocore implies the presence of residual citrate molecules form strong complexation with Fe^{3+} ions, thereby improve the hydrophilicity of nano-core, while $MMCN_{@2.5}$ negative potential attributed to presence of PDA originated phenolic functional groups. Post functionalization with PHMB polymer increased the zeta potential to +40.2 mV, which plausibly explains the successful interface engineering owing to the biguanidine functional groups of PHMB.[21] Raman spectra of $MMCN_{@2.5}$ and PHMB~g~$MMCN_{@2.5}$ were showed (Figure S5, Supporting Information) characteristics peaks at 1345 and 1583 cm^{-1}, attributed to the D band of Sp^3 disordered carbon and G band of Sp^2 graphitic carbon respectively.[10b] In addition, thermogravimetric analysis (TGA) was used to evaluate the grafting of PHMB. As be seen in Figure 2D, the

MMCN$_{@2.5}$ showed no weight loss up to 400 ºC because of its graphitized nature, whereas from 400 ºC to 800 ºC, 17 % weight loss was noted due to subsequent framework carbonization. Moreover, the PHMB~g~MMCN$_{@2.5}$ showed obvious weight loss of 72% starting from 100 ºC to 800 ºC, which could be due to the decomposition of attached PHMB polymer. Therefore, the loading amount of PHMB was about 55%. The magnetic characteristics of magnetic nanocore, MMCN$_{@2.5}$, and PHMB~g~MMCN$_{@2.5}$ were determined by superconducting quantum magnetometer at 300 K (Figure 2E). The results showed magnetic saturation values of 1.34 emu g^{-1}, 0.53 emu g^{-1}, and 0.24 emu g^{-1}, for magnetic nanocore, MMCN$_{@2.5}$, and PHMB~g~MMCN$_{@2.5}$, respectively. In addition, no hysteresis was recorded owing to the well-preserved magnetic core, indicating superior magnetic ability of nanostructures and the presence of nano sized magnetite in core, which favor the ultrafast separation for real-time applications. [10c] The nanoparticles can be easily separated by applying external magnetic force and also aggregated nano-adsorbent can re-disperse by gentle shaking due to its superior hydrophilic nature (inset of Figure 2E).

The X-ray photoelectron spectroscopy (XPS) technique was used to further investigate the elemental composition and chemical state of MMCN$_{@2.5}$ and PHMB~g~MMCN$_{@2.5}$. The wide scan shows four peaks at each spectrum demonstrating the presence of carbon, nitrogen, oxygen and iron without any additional impurities (Figure 2F). A significant increment in the N1$_S$ peak intensity at 399.56 eV was observed in the wide scan after tethering PHMB on the periodic soft-templated mesoporous carbon. This can be attributed to the successful conjugation of the antimicrobial polymer at the interface of MMCN$_{@2.5}$. The higher resolution of MMCN$_{@2.5}$ C1s spectrum showed three distinct peaks located at 284.17 eV, 285.81 eV and 288.67 eV, which assigned to the C-C, C-N, and O-C=O

functional states (Figure 2G). [14b] After surface modification with PHMB the C-N peak were shifted to 285.37 eV and its contents were significantly increased from 21.95 % to 26.82 %. The Figure 2H showed a N1s higher resolution spectrum of $MMCN_{@2.5}$, which revealed the presence of pyridinic, graphitic and oxidized states of nitrogen at 397.92eV, 399.68eV and 402.30eV, respectively. Moreover, the PHMB grafted nanostructure $N1_S$ spectra further deconvoluted and interestingly the peaks were shifted to 397.67 eV, 399.643eV and 401.68eV, while a new biguanide group N peak appeared at 398.60 eV.[22] The quantitative XPS analysis for N element found in $MMCN_{@2.5}$ and PHMB~g~$MMCN_{@2.5}$ was significantly increased from ~7.6 At % to 11.6 At % due to successful conjugation of relatively high N element proportion containing PHMB (Table 1) [22]. The elemental analyzer observations further verified the increase in N element contents from ~2.27 wt % to 10.22 wt % (Table 1), which supports the successful PHMB interface crosslinking over the core-shell nanostructure.

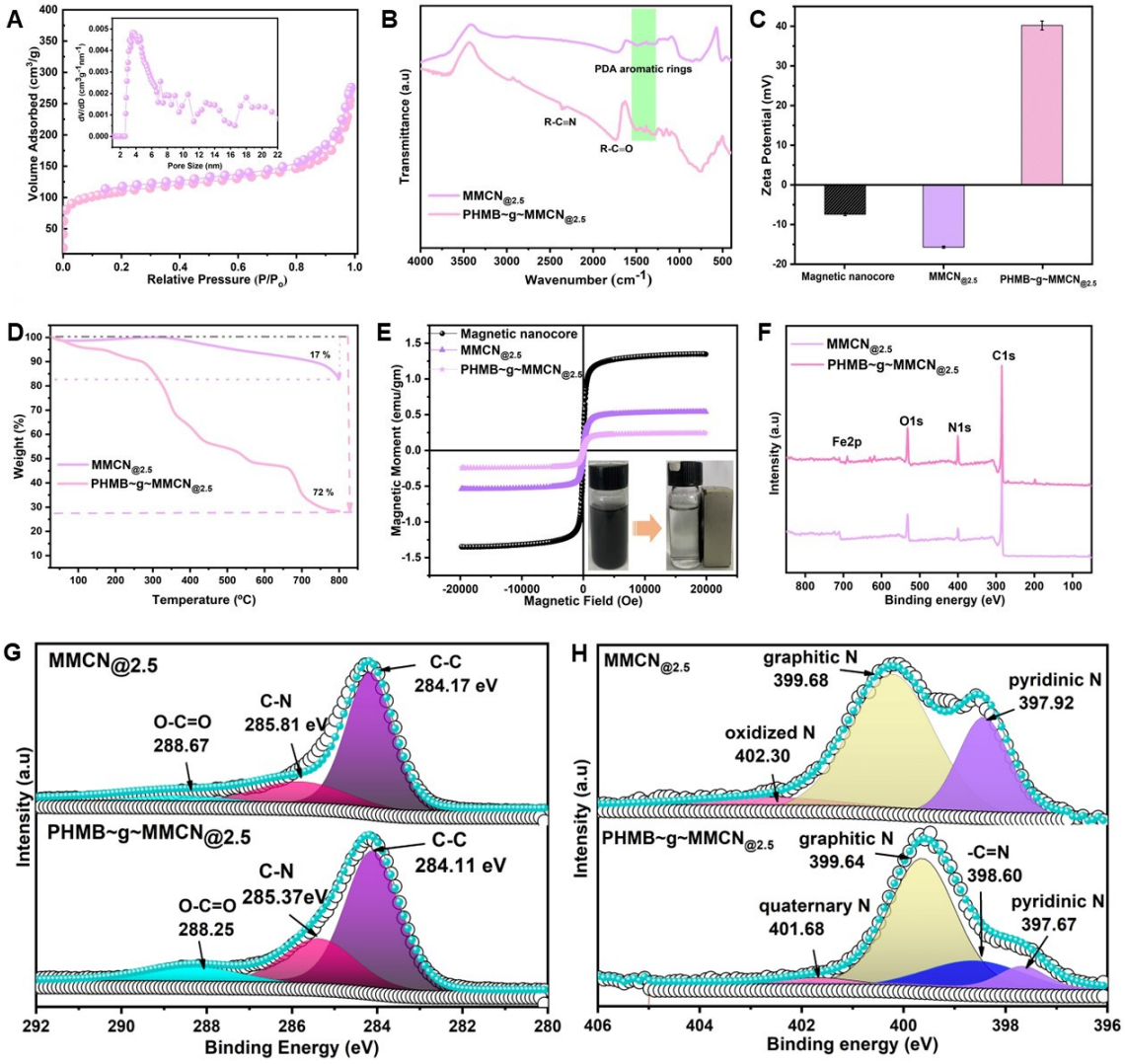

Figure 2. Surface characterizations of the nano-adsorbent. A) N_2 adsorption isotherm and inset pore size distribution, B) FTIR analysis of surface functional groups, C) Zeta potential of magnetic noncore, MMCN$_{@2.5}$ and PHMB~g~MMCN$_{@2.5}$, D) Thermogravimetric analysis, E) Magnetic saturation analysis and inset image of easy separation from aqueous dispersion with external magnetic field, F) XPS wide scan, G) High resolution spectrum of C1s and (H) N1s spectrum of MMCN$_{@2.5}$ and PHMB~g~MMCN$_{@2.5}$.

The magnetic nanocore synthesis process was directed to improve interface depositions of the PDA shell, water dispersibility, biocompatibility and gradient morphology of the nano-adsorbent. The pristine magnetic nanocore synthesized by the traditional solvothermal method showed no affinity for interface deposition of PDA shell resulting in

irregular morphology (Figure S6A, Supporting Information). The uniform nanospheres with mesoporous shell were obtained by encapsulating pristine magnetic nanoparticles with a silica layer by the modified Stöber method. The nonporous silica layer advances the interface deposition of PDA shell by providing -OH groups for tethering F127/DA micelles (Figure S6B, Supporting Information). To avoid the tedious process, alternatively a robust approach of introducing trisodium citrate during the synthesis of magnetic nanocore yields a gradient carboxylate group functionalized nanocore (Figure 1A and S1, Supporting Information). The citrate groups not only act as an electrostatic stabilizer but also provides a better interface for PDA shell by lowering the interfacial energy and producing ordered core-shell nanospheres (Figure S6C, Supporting Information).

Table 1. Elemental composition analysis.

	XPS atomic survey (Atomic %)			**Elemental Analyzer (%)**		
	C	**O**	**N**	**C**	**H**	**N**
$MMCN_{@2.5}$	77.85	12.42	7.6	18.85	0.726	2.27
$PHMB\sim g\sim MMCN_{@2.5}$	74.5	12.64	11.6	30.01	3.932	10.22

To gain further insights into the DA polymerization and TMB-F127-PDA micelles emulsion fusion at the interface of nanocore, $NH_4.OH$ concentration in water/ethanol emulsion was precisely regulated (1~5 mL). The oxidative polymerization of DA begins as NH_4OH introduced into the reaction system and nanocore interfaced deposition of F127-PDA occurs in form of shells. Initially, at 1 mL of NH_4OH, the polymerization of DA produces F127/PDA micelles, which deposited and form shell encapsulating nanocore, which later on turned into a dendritic mesoporous carbon nanosphere and denoted as $MMCN_{@1}$ (Figure 3A). The TEM image of $MMCN_{@1}$ (Figure 3D) showed smaller groves

presence on the core shell structures, furthermore magnified HRTEM observation reveals very thin layer of a PDA shell (~20 nm) deposited directly on nanocore (Figure S7 A and D, Supporting Information). As the concentration of NH_4OH increased (~2.5 mL), rapid PDA and F127 micelles were formed and grows into cylindrical forms, which continuously deposited on magnetic nanocore and resulted in thicker shells growth (Figure 3B). The clear perimeter among nanocore and thicker PDA shells (~39.2 nm) were observed in magnified HRTEM (Figure S7 B and E, Supporting Information), which gave plausible evidence of NH_4OH directed polymerization-controlled assembly of PDA micelle shells. The appropriate amount of NH_4OH promotes the rapid polymerization to match the fusion rate of TMB-F127-PDA micelles alongside of nanocore in a radially aligned cylindrical shape (Figure 3E), which further orderly formed PDA framework and encapsulated the nanocore and transformed into mesoporous nanostructures by carbonization (denoted as $MMCN_{@2.5}$). Generally, increasing amount of NH_4OH (~ 5mL) further increase the rate of DA polymerization and formation of thicker PDA shells (~54.5 nm) (Figure S7 C and F, Supporting Information), which increase the surface interfacial energy and resulted in the week adherence and increased critical micelle concentration or complete breakdown of PDA shell by exposing nanocore (Figure 3C and F), which ultimately decreased the BET surface area as reported in Table 2. The average particle size increased from 240 to 274 nm as the concentration of NH_4OH increased from 1 mL to 5 mL (Figure 3G-I). The resultant BET surface area of samples was summarized in Table 2 and graphical representation was also showed (Figure S8, Supporting Information). Interestingly, the amount of NH_4OH was found to be an important factor in micelles directed assembly and determines the morphological features, surface area and the size of nanoparticles.

Table 2. Texture properties of the core-shell carbon nanostructures.

Sample	S_{BET} ($m^2 g^{-1}$)	Pore Volume ($cm^3 g^{-1}$)	Pore Size (nm)	Particle size (nm)
$MMCN_{@1}$	112.74	0.272	10.02	~240
$MMCN_{@2.5}$	421.24	0.379	13.45	~260
$MMCN_{@5}$	256.74	0.102	9.98	~274

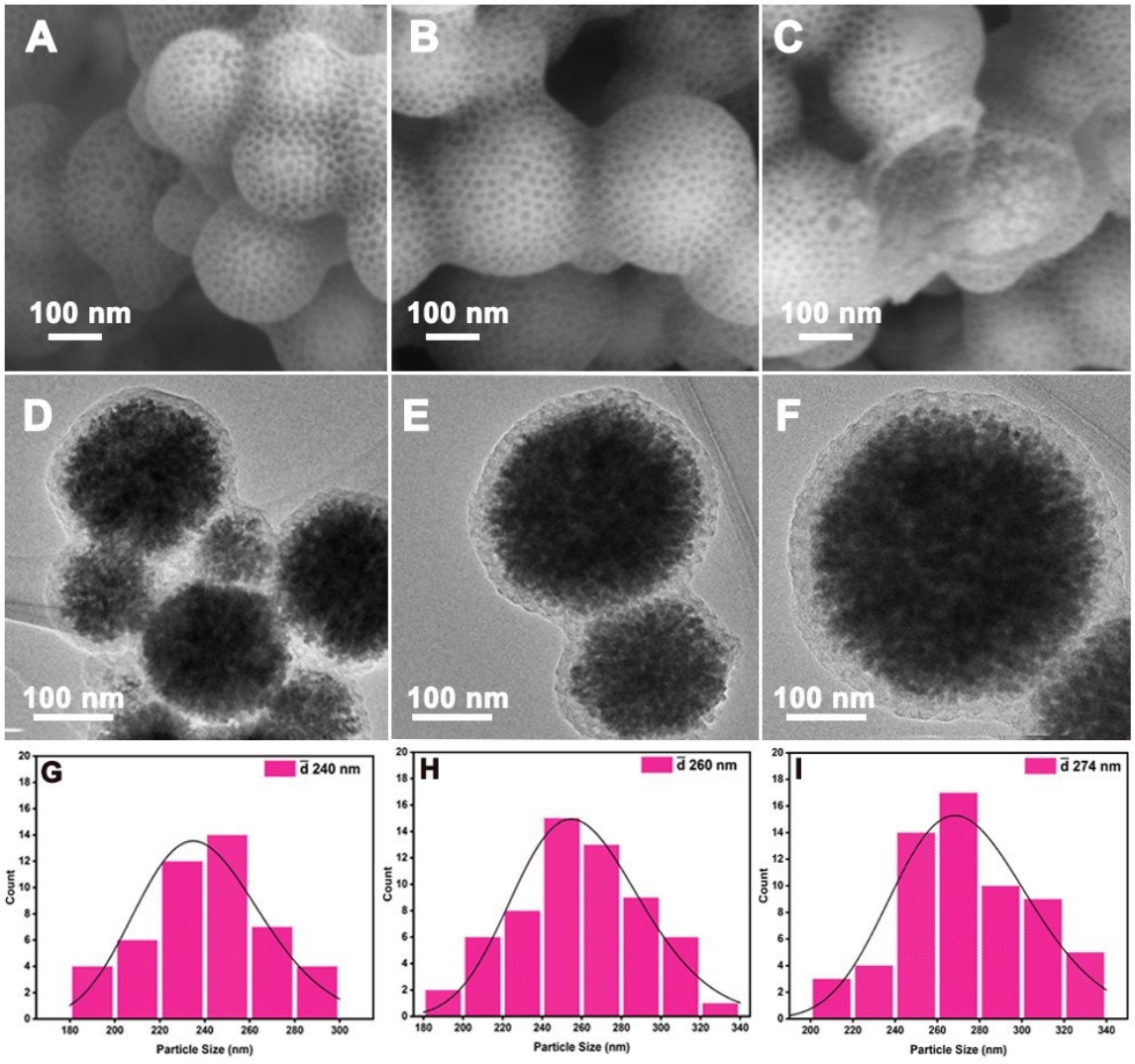

Figure 3. The NH_4OH amount regulated evolution of structural and morphological variations during nanocore interface co assembly of F127-PDA micelle. A and D) FESEM and TEM images of $MMCN_{@1}$, B and E) FESEM and TEM observations of $MMCN_{@2.5}$, C and F) FESEM and TEM of $MMCN_{@5}$, G-I) Corresponding nano size distribution histograms at increasing concentrations of NH_4OH.

Batch adsorption experiments were systematically conducted to gain insight into Tl(I)

uptake performance of PHMB~g~MMCN$_{@2.5}$ in terms of adsorption kinetics, adsorption capacity, the effect of pH, influence of interfering ions, and reusability. The adsorption kinetics parameter provides insightful information about adsorption process to determine the rate-limiting steps, mass transfer, and mechanism of adsorption.[23] As can be seen in Figure 4A, the PHMB~g~MMCN$_{@2.5}$ exhibited a faster adsorption rate, and adsorption equilibrium reached within 60 min. Initially, the adsorption kinetics data were analyzed by mass transfer models including *pseudo*-first order (Eq. (3)) and *pseudo*-second order model (Eq. (4)) to interpret the mass transfer mechanism and phenomena by favorable tailor-made structure of nano-adsorbent (Figure 4A). The correlated parameters of kinetic models were summarized in Table. 3. The adsorption kinetic data best fitted by *pseudo*-second order model with higher correlation coefficient (R^2) of 0.997 as compared to first order R^2 of 0.904, which indicates the chemisorption nature of the adsorption process.[24]

Table 3. Fitted parameters of adsorption kinetics models of TI (I) on PHMB~g~MMCN$_{@2.5}$.

***Pseudo* first order**			***Pseudo* second order**		
Q_e (mg g^{-1})	k_1 (min^{-1})	R^2	Q_e (mg g^{-1})	K_2 (g mg^{-1} min^{-1})	R^2
51.65	32.26	0.9048	55.377	0.009	0.997

In addition, the Weber-Morris Intraparticle Diffusion model (Eq. (5)) was also fitted on the adsorption data to determine rate-limiting steps of the adsorption process and devise the mechanism of adsorption. As can be seen from Figure 4B, the removal of Tl(I) process involved three distinct regions and a multilinear plot was drawn from adsorption kinetic data fitted by the Weber-Morris Intraparticle Diffusion model. The data fitting curves of the plot showed that the adsorption process involved following phases: (i) external diffusion phase in which Tl(I) ions formed a layer on the external surface of

PHMB~g~MMCN$_{@2.5}$ by diffusion from solution, (ii) internal diffusion phase ascribed the intraparticle diffusion of Tl(I) ions further inside of pores or capillaries of the internal structure of PHMB~g~MMCN$_{@2.5}$, (iii) equilibrium phase was involved in the chemical sorption and saturation of binding sites with Tl(I) ions. The plot of Q_t vs $t^{0.5}$ shows the linearity of all three slopes and transverse through the origin indicating that the Weber-Morris Intraparticle Diffusion model is responsible for controlling the adsorption process. The simulated parameters from slope and intercept were listed in Table 4. The intraparticle diffusion constant (K_p) values were decreased in the order of $Kp_1 > K_{p2} > K_{p3}$, which suggests that the internal diffusion is closely linked to the adsorption process.[25]

Table 4. Simulated parameters of intraparticle diffusion model of Tl uptake by PHMB~g~MMCN$_{@2.5}$

K_{p1} (mg g^{-1} min^{-1})	C (mg g^{-1})	R^2	K_{p2} (mg g^{-1} min^{-1})	C (mg g^{-1})	R^2	K_{p3} (mg g^{-1} min^{-1})	C (mg g^{-1})	R^2
3.72	32.15	0.90	0.12	52.22	0.97	0.04	53.84	0.98

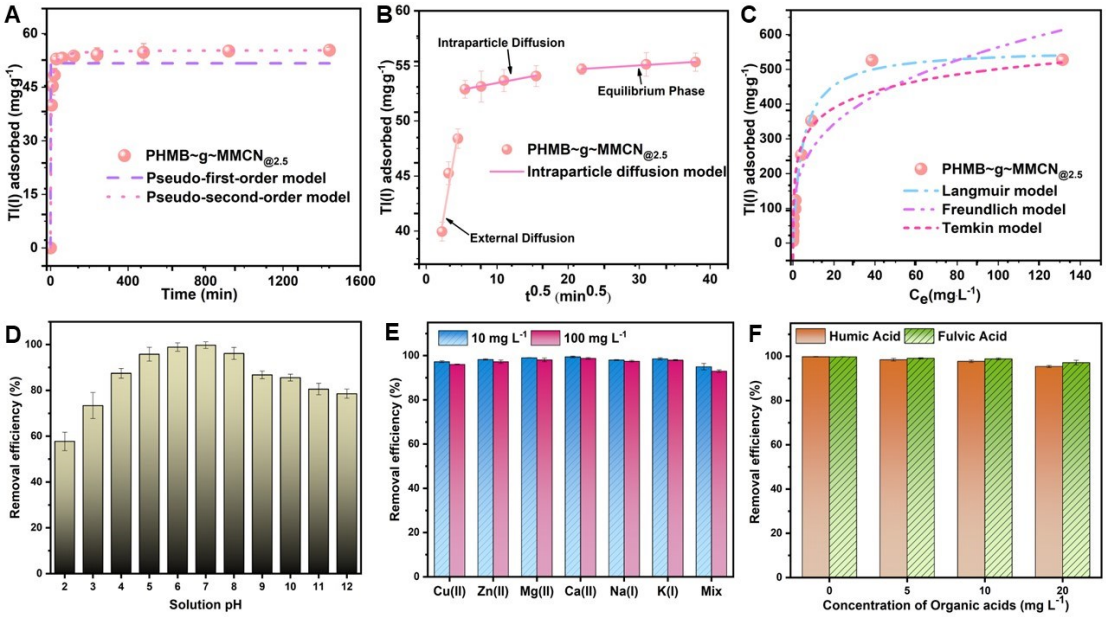

Figure 4. Adsorption performance of nano-adsorbent. A-B) Adsorption kinetics for Tl(I)

ions using the mass transfer models and Weber-Morris Intraparticle Diffusion model, respectively, C) Adsorption isotherms for Tl(I) onto PHMB~g~MMCN$_{@2.5}$, D) Effect of initial pH (2.0−12.0) on Tl(I) removal, E) Effect of coexisting cations on Tl(I) removal by PHMB~g~MMCN$_{@2.5}$ (initial cations concentration: 10 or 100 mg L^{-1}; "Mix" denoted to the mixture containing seven interfering ions of equal concentration), F) Influence of interfering dissolved organic acids on Tl(I) ions removal .

The adsorption isotherm studies define the nature of interaction among adsorbate removal amount (Qe) and remaining concentration (Ce) after attaining equilibrium.[26] The adsorption parameters were key to determine the theoretical adsorption capacity (Qm) and interpret the adsorption behavior. [27] Figure 4C shows the Tl(I) equilibrium adsorption isotherms on PHMB~g~MMCN$_{@2.5}$ with associated fitting curves of the Langmuir, Freundlich and Temkin isotherm models, while calculated parameters of each model were listed in Table 5. The Langmuir isotherm model provides a better fit for Tl(I) removal on PHMB~g~MMCN$_{@2.5}$, suggesting Tl(I) actively adsorbed on sites with fixed energy distribution and formed monolayer. The maximum adsorption capacity of Tl(I) calculated by the Langmuir isotherm model on PHMB~g~MMCN$_{@2.5}$ at pH= 7.0 and 25 °C is to be 559.49 mg g^{-1}, which is nearly identical to the experimental adsorption capacity (Qe) of 526.31 mg g^{-1}. Moreover, the representative correlation coefficient (R^2) of Langmuir isotherm model is 0.998, which is much higher as compared to Freundlich (0.908) and Temkin models (0.915). The PHMB~g~MMCN$_{@2.5}$ efficiency for Tl(I) uptake surpassed a series of adsorbents reported in the literature (Table S2, Supporting Information). For example, Haris et al.[24] synthesized exfoliated biochar-based adsorbent for selective adsorption of Tl(I) metal. The lower apparent adsorption performance as compared to PHMB~g~MMCN$_{@2.5}$ were associated with irregular morphology of biochar nanosheets and smaller pore size (3.98 nm), while the adsorbent was not easy to separate from aqueous matrices due to lack of magnetic property. It can be speculated that the higher adsorption

amount of Tl(I) is credited to the synergistic effects of fast diffusion due to ordered mesoporous structure and higher N functionalities on the surface and pore wall (Figure 1).

Table 5. Fitted parameters of adsorption isotherms of Tl(I) ions uptake by PHMB~g~MMCN$_{@2.5}$

Langmuir model			**Freundlich model**			**Temkin model**		
Q_{max} (mg g^{-1})	k_L(L mg^{-1})	R^2	K_F (L g^{-1})	1/n	R^2	k_T (L g^{-1})	b (KJ mol^{-1})	R^2
559.49	0.214	0.998	13.031	0.308	0.90	13.517	69.457	0.91

Solution pH is among very important parameters in the adsorption process due to its direct relation with the adsorbent surface functional sites charge and metal speciation.[28] The effect of solution pH on Tl(I) ions uptake was studied in the range of 2.0 to 12.0, and the obtained results were showed in Figure 4D. As can be seen, the Tl(I) ions removal efficiency increased (57 %~99 %) as the pH increased from acidic to basic. However, at high pH, the sorption efficiency decreased, which could be due to weak alkaline conditions of PHMB~g~MMCN$_{@2.5}$. The lower adsorption amount of Tl(I) ions under acidic conditions can be attributed to the competitive adsorption among H^+ ions and Tl(I) ions, and the protonation of adsorbent surface functional moieties. Furthermore, as the pH increased from acidic to basic, the deprotonation of adsorbent surface and lower concentration of H^+ ions in the solution resulted in higher sorption efficiency of Tl(I) ions.[24] The Tl(I) ions sorption is very persistent and the highest adsorption (>99 %) take place at the pH of 7.0, which is due to the presence of dominant Tl(I) species in the solution and its stable nature over a wide pH range.[29]

The interfering ions capabilities of the PHMB~g~MMCN$_{@2.5}$ were further

systematically analyzed. As showed in Figure 4E, the PHMB~g~MMCN$_{@2.5}$ demonstrated nearly 96 % of Tl(I) ions adsorption efficiency in the presence of 10 and 100 mg L^{-1} of six coexisting divalent and monovalent cations (e.g., Cu(II), Zn(II), Mg(II), Ca(II), Na(I), and K(I)). Moreover, the removal efficiency of Tl(I) ions is also investigated from a solution containing a mixture of the above interfering ions, which is nearly above 92 %. The hydration free energy of Tl(I) is − 300 kJ/mol (Table S3, Supporting Information), which is much lower than the hydration free energy of other common ions,[30] implying a weak interaction between Tl(I) and the water molecules of its hydration shells. Therefore, Tl(I) easily reduces the number of water molecules in their hydration shells and could easily enter into open ended pores. The decrease in adsorption efficiency was attributed to the specific affinity of adsorbate molecules towards functional moieties (e.g., -OH, -COOH, -NH_2) present on adsorbent surface, which were due to specific ionic potential, electronegativity and ionic radius.[31] The Cu(II) and Zn(II) ions exhibit relatively higher electronegativity values in contrast to targeted Tl(I) ions (Table S3, Supporting Information), which resulted in stronger interference at the functional sites. Furthermore, K(I) ions have similar hydrated ionic radii as Tl(I) ions.[32] Hence, mild interference for adsorption sites was also observed in the binary solution of K(I) and Tl(I) ions.

Dissolved organic acids (DOMs) are commonly found in natural and industrial water metrices and can potentially hinder the adsorption process of targeted metal ions from complex aqueous environment. Humic acid and fulvic acid are usually considered as model DOMs, since they produced dissolved organic carbon contents of about 10 % and 40 %, respectively.[33] Generally, organic acids have abundant of aromatic, phenolic and carboxylic binding sites and form stable complexes with metal ions. [33b] Hence, the

systematic investigation about the effect of coexisting DOMs on Tl(I) removal by PHMB~g~MMCN$_{@2.5}$ is imperative to define adsorbent efficiency. As illustrated in Figure 4F, the existence of humic and fluvic acids in the range of 0 to 20 mg L^{-1} removal of Tl(I) with decrease in adsorption efficiencies of about 5 % and 3 %, respectively. Herein, humic acid interference in removal of Tl(I) ions were slightly higher because of the formation complexes. Overall, the tremendous anti-interfering DOM capability of PHMB~g~MMCN$_{@2.5}$ suggests possible application for real water matrices.

The antimicrobial activities of MMCN$_{@2.5}$, PHMB and PHMB~g~MMCN$_{@2.5}$ were determined by minimal inhibitory concentration (MIC) and killing ratio test against Gram-positive (*S. aureus*) and Gram-negative (*E. coli*) bacterial strains. The PHMB~g~MMCN$_{@2.5}$ possess excellent antimicrobial potency with low MIC in the range of 1-2 μg mL^{-1} and 2-4 μg mL^{-1} towards *S. aureus* and *E. coli*, respectively (Figure S9, Supporting Information). Thus, the dosage of materials varied from 0 μg mL^{-1} to 3.0 μg mL^{-1}, while the initial concentration of both bacterial strains was kept at ~10^7 CFU mL^{-1}. Figure 5A and B showed the plots of *S. aureus* and *E. coli* visible bacterial colony counts versus increasing dosage of MMCN$_{@2.5}$, PHMB and PHMB~g~MMCN$_{@2.5}$, and Figure 5C shows the images of surviving bacterial colonies on agar plates after treatment. The number of colonies of *S. aureus* and *E. coli* were reduced to ~ 10^3 CFU mL^{-1} after PHMB~g~MMCN$_{@2.5}$ treatment and MIC were as low as 2 ug mL^{-1} (>99.9% killed) and 2.5 ug mL^{-1} (>99.99% killed), respectively. The pristine MMCN $_{@2.5}$ showed insignificant antimicrobial performance, while PHMB exhibited certain antimicrobial activity against *S. aureus* and *E. coli*, the killing efficacies were 96.2 ± 1.8 % and 99.8 ± 0.1 % respectively at the dosage of 3.0 ug mL^{-1} mainly from free PHMB.[22] However, PHMB~g~MMCN$_{@2.5}$

significant increase in bactericidal efficiency could be due to PHMB improving the adhesion of PHMB~g~MMCN$_{@2.5}$ to bacterial cell wall and promoting the penetration of the bacterial cell wall by physical or chemical strategies leading to bacterial leakage. Interestingly, Zan et al. [21] also reported similar results, where have modified Au nanoparticle by PHMB and used them for antimicrobial purposes for biofilm eradication. Furthermore, a systematic disinfection kinetics study of nano-adsorbent was conducted with increasing contact time from 0 min to 10 min and results can be seen in Figure 5D. The optical images of *S. aureus and E. coli* showed ultrafast disinfection capability of PHMB~g~MMCN$_{@2.5}$, and inhibition rate of 99.99 % achieved with in 4 min for both bacterial strains.

Primarily, to determine the real-time application potential of PHMB~g~MMCN$_{@2.5}$ as a dual-functional water decontamination agent, its performance was further investigated in pollutant simulated deionized and lake water. The water matrices were sterilized by autoclaving and then inoculated with ~10^6 CFU mL^{-1} concentrations of *S. aureus and E. coli* and 5 mg L^{-1} of Tl(I) metal ions. The above treatments were loaded with 2 mg of PHMB~g~MMCN$_{@2.5}$ nano-adsorbent except for the controls for each bacterial strain. Figure 6A showed an excellent water purification capability of PHMB~g~MMCN$_{@2.5}$ in pollutant spiked deionized water and over 99.1 % of Tl(I) was successfully removed. In addition, the disinfection performance of PHMB~g~MMCN$_{@2.5}$ revealed a killing efficiency of over 99.99 % for both bacterial strains, which can also be observed in optical images of bacterial colonies before and after treatment (Figure S10, Supporting Information).

Furthermore, the capability of PHMB~g~MMCN$_{@2.5}$ for simultaneous adsorption and

disinfection was investigated in real-time application scenario of pollutant spiked lake water. As displayed in Figure 6B, the nano adsorbent can effectively uptake Tl(I) from pollutant simulated lake water and achieve 91% removal efficiency. The slight decrease in adsorption efficiency could be attributed to the complex matrix presence in lake water that may hinders the adsorption process by competing for adsorption sites.[8c, 34] The organic material found in natural water have the ability to confine the Tl(I) ions by forming complexes, which could further restrict the adsorption process.[35] Moreover, the Figure 6B showed that the killing efficiency of initially inoculated *S. aureus and E. coli* concentrations of ~10^6 CFU mL^{-1} were as high as 99.99 %, which can be further visualized by optical images of bacterial colonies after treatment (Figure S10, Supporting Information). The above results suggest that the performance of PHMB~g~$MMCN_{@2.5}$ for simultaneous water purification in various water matrices has the upscaling potential for real time applications.

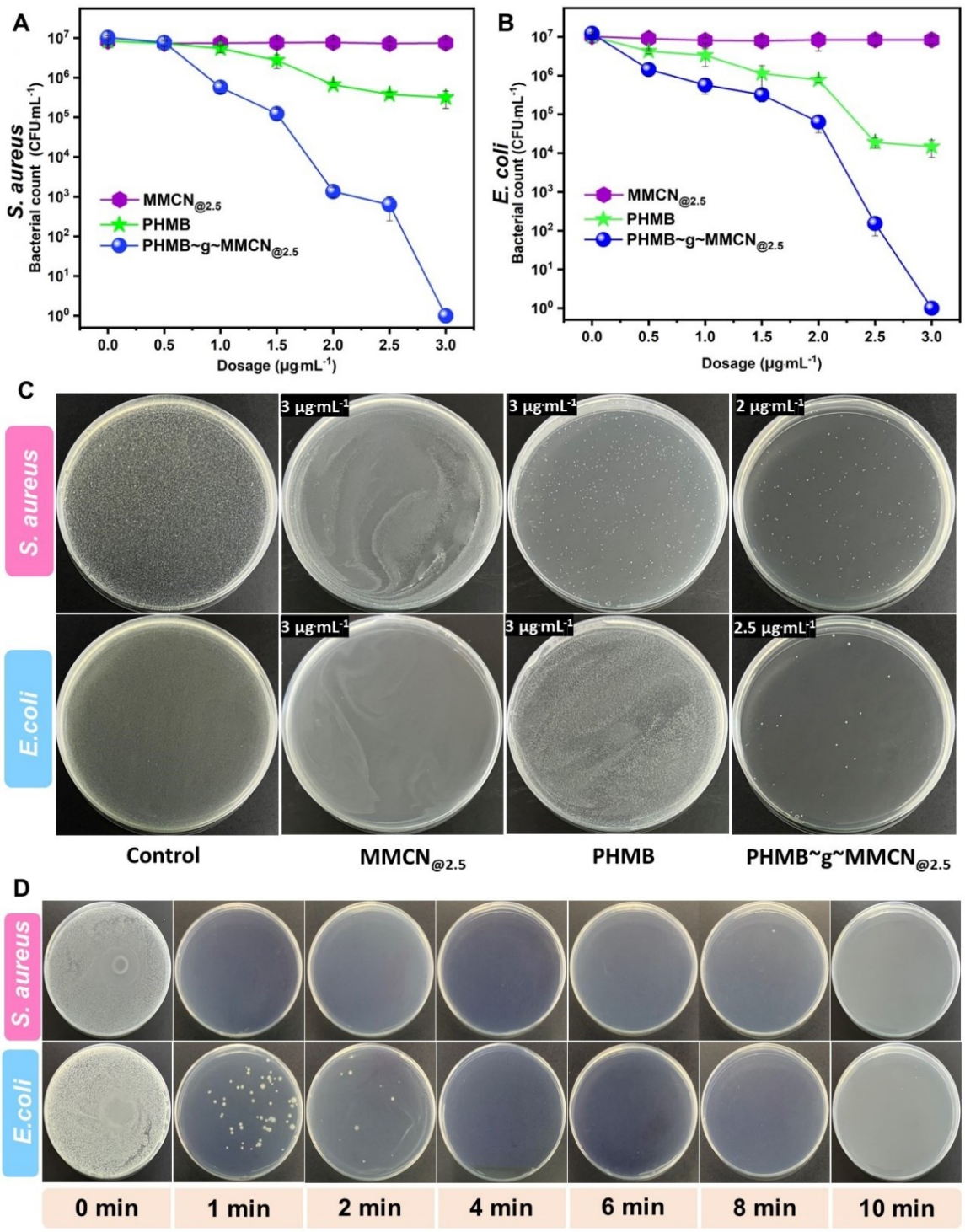

Figure 5. Disinfection performance of nano adsorbent. A-B) Count of viable *S. aureus* and *E. coli* versus the increase of MMCN$_{@2.5}$, PHMB, and PHMB~g~MMCN$_{@2.5}$ material dosage, C) Optical images of *S. aureus* and *E. coli* colonies detected under different dosage of materials, D) Optical images of ultra-fast disinfection kinetics of *S. aureus* and *E. coli* by PHMB~g~MMCN$_{@2.5}$.

The recycling capability of nano-adsorbent after being used for adsorption and disinfection is a very important parameter for long-term efficient application. Therefore, continuous adsorption-desorption and disinfection experiments were performed to evaluate the efficiency of nano-adsorbent as a water purifier. Figure 6C, displayed the Tl(I) removal efficiency of PHMB~g~MMCN$_{@2.5}$ for six consecutive cycles and nano-adsorbent is capable to maintain >82 % adsorption efficiency. The decrease in performance efficacy could be due to Tl(I) adsorbed on the active sites has not been completely desorbed, resulting in a relative decrease in the number of active sites for succeeding adsorption cycles. Furthermore, the regenerated nano-adsorbent disinfection ability was also assessed for six consecutive cycles as showed in Figure 6D. The disinfection efficiency of PHMB~g~MMCN$_{@2.5}$ towards *S. aureus and E. coli* showed excellent bacterial inhibition of >99.99 % even after five consecutive cycles. The optical images of cultured bacterial strains of control and after treatment were showed in Figure S11 in the supporting information. The excellent recyclability and easy separation by external magnetic field render us to believe that PHMB~g~MMCN$_{@2.5}$ is a highly stable nano-adsorbent and has great potential for water decontamination applications.

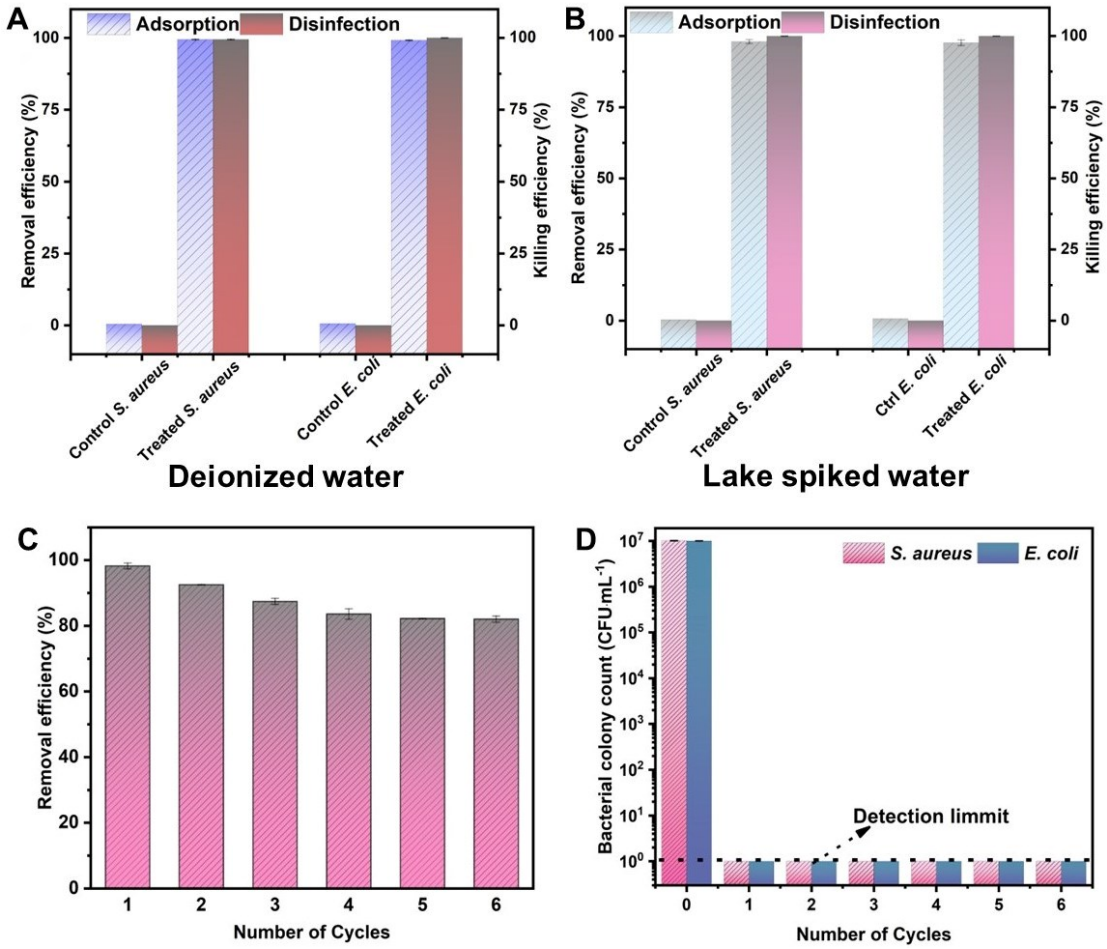

Figure 6. Simultaneous water purification and reusability performance. A-B) Simultaneous removal efficiency of Tl(I) ions and killing efficiency towards *S. aureus* and *E. coli* in deionized water and Spiked Lake water, respectively, C) Cyclic adsorption performance of Tl(I) ions, D) Cyclic *S. aureus* and *E. coli* disinfection performance.

The adsorption and disinfection mechanism identification are one of the most significant fundamental principles necessary to bridge the gap between water purifications investigations and engineering design. The mechanism of Tl(I) ions adsorption on the surface PHMB~g~MMCN$_{@2.5}$ was deeply investigated by XPS before and after adsorption as illustrated in Figure 7A. The wide scan peaks appear at 284.8, 400.15, 531.7 and 710.8 eV binding energies were the characteristic peaks of C $_{1s}$, N $_{1s}$, O $_{1s}$ and Fe $_{2p}$ respectively. The new peak appeared after the adsorption of the metal ion at 119.04 eV, which is the characteristics peak of Tl(I) species. This proved the successful uptake of Tl(I) ions. Figure.

7B represent the core level spectrum of Tl $_{2p}$, the peak deconvoluted into two binding energies at 118.87 eV and 123.35 eV corresponding to Tl $4f_{7/2}$ (58.26 %) and Tl $4f_{5/2}$ (41.74 %), respectively. The peak fitting analysis of O1s before and after Tl(I) adsorption are showed in Figure 7C. It can be observed that O 1s spectrum includes three peaks at the binding energies of 529.13 eV, 530.31 eV and 531.80 eV, reflected to -O, -OH, and H_2O respectively. The peaks shift was reported after the adsorption of Tl(I) ions and the relative element contents of OH reduced from 66.84 % to 55.51 %, suggesting that the hydroxyl groups participated in the adsorption process and coordinated and chelated with Tl(I) ions. Furthermore, N1s spectrum analysis after adsorption showed peak shift of CN ligand (Figure 7D), which could be due to Tl(I) approach to the CN functional sites and lower the electron density around N atoms and subsequent increase in binding energy.[36]

To explore the antimicrobial mechanism of the PHMB~g~$MMCN_{@2.5}$ from the morphology of bacteria, the integrity of the bacterial cell wall was evaluated by the SEM method (Figure 7E). The SEM observations of controls of *S. aureus and E. coli* showed intact and smooth globular and rod-like cell membrane morphologies. After treatment with PHMB~g~$MMCN_{@2.5}$, the outer membranes of *S. aureus and E. coli* integrity compromised shrivelled or collapsed with massive of intracellular matrix leaked from the bacteria.[13] This could be attributed to the fact that nano-adsorbent surface attached PHMB perforate bacterial cell membrane through an electrostatic interaction, which make membrane more porous leading to the lethal leakage of cytoplasmic substances by contact sterilization.[37]

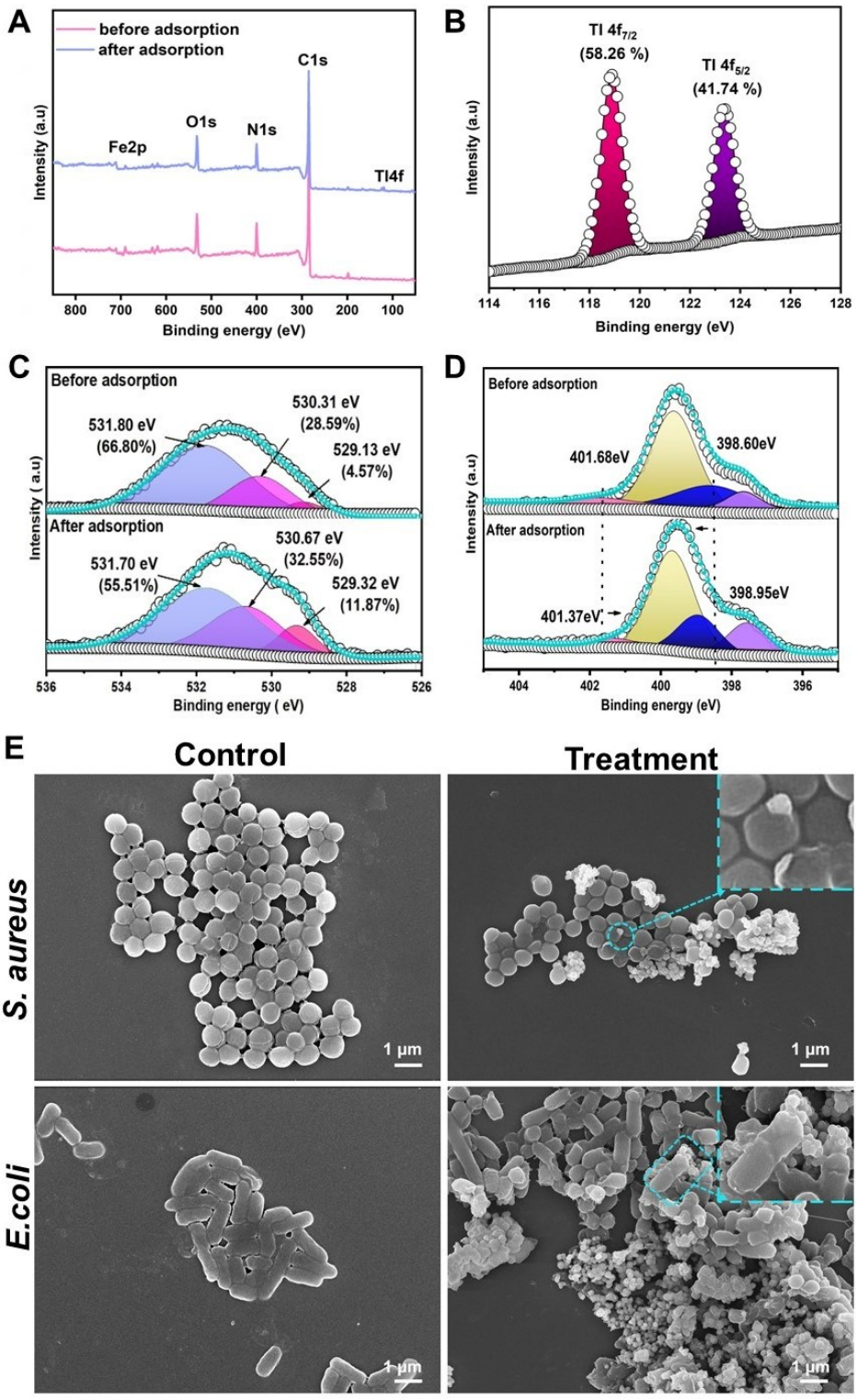

Figure 7. Adsorption and disinfections mechanism insight**.** A) XPs wide scan spectrum before and after Tl(I) adsorption, B) High-resolution Tl 4f spectrum, C) High resolution spectrum of O1s before and after adsorption of Tl(I), D) High resolution spectrum of N1s before and after adsorption of Tl(I), E) SEM observations of *S. aureus* and *E. coli* before

and after treatment (inset high resolution images of nano-adsorbent interfacing bacterial cell wall).

From XPS peak fitting results of O1s and N1s, the adsorption mechanism was drawn and showed in Scheme 2. The -OH and -CN provides electron lone pair, which combines with Tl(I) and forms a stable chelate complex. In addition, 3D aligned symmetrical pores diameter is higher than the hydrated diameter of Tl(I) (0.66 nm), which also facilitate the diffusion of metal ions inside to the magnetic core and formed an inner sphere complex with Tl(I) ions. In addition, the disinfection mechanism attributed to the cell wall depolarization and disruption by non-specifically binding fatty acid, breaking the charge and permeability balance of the bacterial membrane due to the biguanidine groups of antimicrobial PHMB. The membrane phospholipid head group interact with hydrophilic biguanidine groups of nano-adsorbent and partially penetrate inside. Afterwards, the polymer could easily reduce the membrane fluidity, ions, ATP, and potentially block DNA replications process, which cause cell lysis.

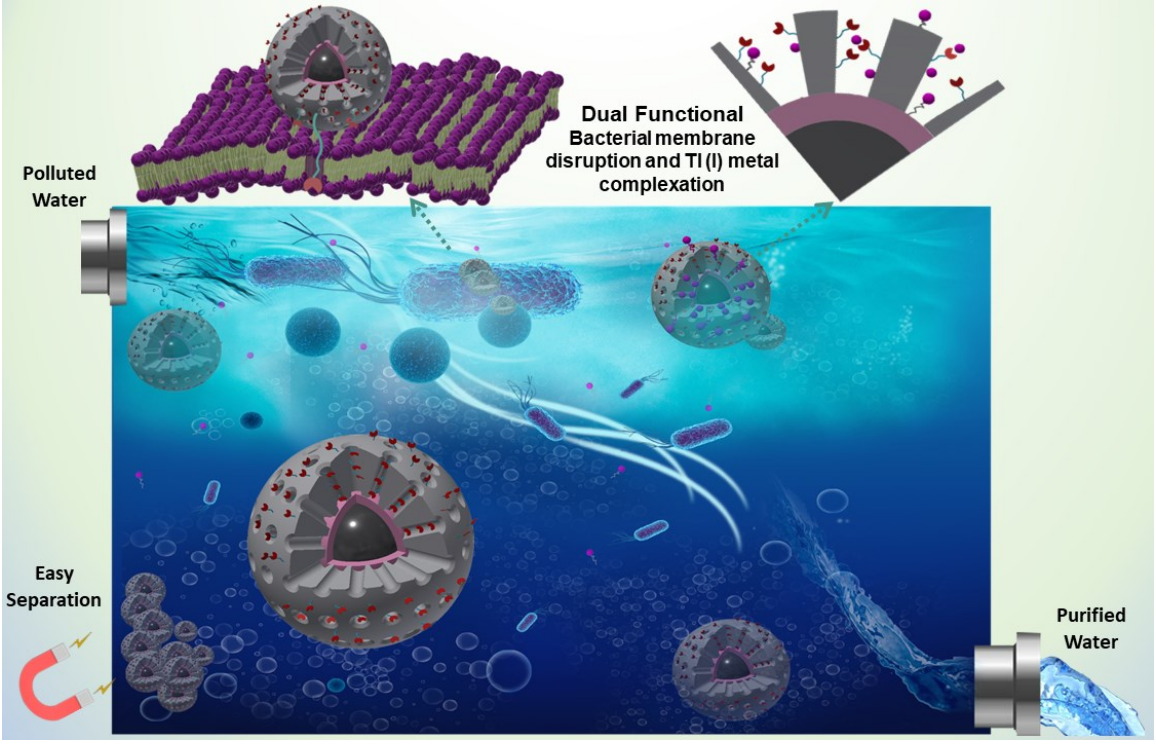

Scheme 2. Schematic diagram of the water purification of nano-adsorbent.

3. Conclusion

In summary, we developed a novel class of nano-adsorbent for water purification that can effectively adsorb toxic Tl(I) and simultaneously kill bacteria. The $MMCN_{@2.5}$ with unique mesoporous core-shell architectures and gradient pores have been rationally synthesized by emulsion-induced assembly approach. The nanostructure was programmatically tuned by adjusting the NH_4OH amount, which resulted in the controllable pore sizes, surface area, pore volume and nanoparticle size. The antimicrobial PHMB polymer was successfully tethered on the mesoporous PDA derived shell to induce the disinfectant capability. The resultant gradient-pore PHMB~g~$MMCN_{@2.5}$ show uniform particle size (~260 nm), high surface area (~363.47 m^2g^{-1}), large pore volume (~0.426 cm^3g^{-1}) and 3D open pore configuration. As a result, the gradient-porous

PHMB~g~MMCN$_{@2.5}$ exhibits promising Tl(I) removal capability (~559 mg g^{-1}), exceptional disinfection performance against *S. aureus* and *E. coli* (killing efficiency >99.99%.), ultrafast disinfection kinetics rate (within ~4 min), and significant recyclability. In addition, the nano adsorbent embarked excellent dual functionality of adsorption and disinfection performance in deionized and lake water. We envisage that this unprecedented programmable emulsion-induced interface dynamic assembly method would pave a new avenue to constructing mesostructured objects with high level of functionality and complexity.

4. Experimental Section

Chemicals: The chemicals used in this study were provided in the supplementary information (SI) text.

Synthesis of Magnetic core: Highly water dispersible magnetic nanocore with trisodium citrate residues in size was prepare as reported previously.[38] In detail, $FeCl_3$ (0.325 g) and trisodium citrate (1.0 g) were dissolved in ethylene glycol (20 mL). Afterward, NaAc (1.2 g) was added to the mixture and solution was stirred for 30 min and transferred into a Teflon lined stainless steel autoclave. The autoclave was heated at 200 °C for 10 h and then cooled to room temperature (25 °C). The obtained magnetic nanocore particles were washed with milli Q water and ethanol repeatedly. Furthermore, Fe_3O_4@SiO_2, with nonporous silica shell was prepared by modified Stöber method.[39] The aqueous dispersion of Fe_3O_4 (2 mL, 40 g/mL) in water (35 mL) and ethanol (105 mL) emulsion and NH_4OH (2.0 mL) under mechanical stirring. After 30 min (2.79 g) TEOS was added and stirred for 8 h and later washed with milli Q water and ethanol several times.

Controlled self-assembly of PDA shell: Briefly, 100 mg of F127 and 0.1 mL TMB was

added in milli Q water (5 mL) and ethanol (4.7 mL) emulsion by ultrasonication. Afterwards, 20 mg of magnetic nanocore and 120 mg of DA dispersion in ethanol (0.3 mL) was added under mechanical stirring (280 rpm) at 25 ºC. After 1h, a specific amount of NH_4OH (28 wt%) was dropwise added to regulate the fusion of TMB/F127/DA micelles, and the reaction will allow to proceed for another 2 h. The nanostructure was separated by magnets, followed by washing with milli Q water and ethanol. The amount of NH_4OH (28 wt%) was regulated to 1 mL, 2.5 mL and 5 mL and resultant nanostructures was denoted as ($MMCN_{@X}$) accordingly (Here x is the amount of NH_4OH). After drying at 60 ºC in vacuum, the as-made sample ($MMCN_{@X}$) was carbonized at 300 ºC in N_2 atmospheres at a heating rate of 1 ºC $\cdot min^{-1}$ for 1 h, and further raised to 550 ºC at a heating rate of 1 ºC $\cdot min^{-1}$ and kept for 2 h.

Surface Cross-linking of $MMCN_{@2.5}$ by PHMG: Typically, the DMF (5 mL) and PHMB (1 mL) were added in a round bottom flask under mechanical stirring (280 rpm) followed by addition of $MMCN_{@2.5}$ (25 mg) and 4-dimethylaminopyridine (0.927 mg) and the reaction was cooled to 0 °C in an ice bath. The solution of DCC (39.14 mg) in DMF (2 mL) was dropwise added and stirred for another 2 h under the ice bath. Afterwards, the solution was mechanically stirred for another 8 h at room temperature. Finally, the as made nanostructures were washed with milli Q water and ethanol several times and PHMB-g-$MMCN_{@2.5}$ was obtained by lyophilization.

Characterization: The detailed characterization methods were discussed in the supplementary information (SI) text.

Batch Adsorption: To examine adsorption kinetics study, 200 mg PHMG~g~$MMCN_{@2.5}$ was weighted and suspended in 500 mL volume of 20 mg L^{-1} Tl(I) concentration solutions

and 5 mL samples were withdrawn after specific time intervals. The adsorption isotherm study was measured by adding 20 mg of PHMG~g~MMCN$_{@2.5}$ into 50 mL solution of Tl(I) ions with varying concentrations range between 2.5 to 350 mg L^{-1}. The solution pH was adjusted to 7.0 at 25 ◦C ± 5 and shaken for 24 h to achieve equilibrium. The effect of pH was studied by suspending 20 mg nano adsorbent in 20 mg L^{-1} Tl(I) concentration solution having 50 mL volume and pH was adjusted between 2.0 to 12.0 by 0.1 M HCl and NaOH, respectively. The effect of interfering monovalent (Na(I), and K(I)) and divalent cations (Cu(II), Zn(II), Mg(II)) competitive adsorption were examined from a solution exhibiting 10 and 100 mg L^{-1} concentrations of individually and in mixed state with initial Tl(I) concentration of 10 mg L^{-1}. To examine the dissolved organic acid interference, a batch adsorption study was conducted containing 0 to 20 mg L^{-1} humic and fulvic acids, 10 mg L^{-1} Tl(I) concentrations and 10 mg adsorbent. For regeneration of spent adsorbent during the adsorption of Tl(I) ions, 10 mg adsorbent were suspended in a series of 25 mL solutions containing 20 mg L^{-1} Tl(I) metal ions and shaken for 8 h at 25 ◦C ± 5. After equilibrium the spend adsorbent was separated by external magnet and again redispersed in a 0.1 M Na_2EDTA eluent for another 4 h in a thermostat shaker at 25 ◦C ± 5. The regenerated nano adsorbent was repeatedly washed with ethanol and milli Q water and dried in freeze dryer for succeeding cycle application. The residual concentration of Tl(I) was determined by ICP-OES analysis. The adsorbed metal per unit mass of PHMG~g~MMCN$_{@2.5}$ (mg g^{-1}) was determined according to Equation 1 and removal percentage (%) was concluded by Equation 2:

$$q_e = \frac{(c_i - c_e)v}{M} \quad (1)$$

$$R \cdot E\% = \frac{c_i - ce}{c_i} \times 100 \quad (2)$$

Where q_e (mg g^{-1}) corresponded to maximum adsorption capacity at equilibrium. C_i is initial metal ions concentration, C_e is the metal ions at equilibrium liquid-phase (mg L^{-1}), while m and V is the adsorbent weight (g) and the volume of the solution (L), respectively.

Adsorption Kinetics and isotherm modelling: Adsorption kinetic data were fitted by nonlinear *pseudo* first rate order (Equation 3), *pseudo* second rate order (Equation 4), and Weber-Morris Intraparticle Diffusion model (Equation 5):[40]

$$q_t = q_e(1 - e^{(-k1t)}) \quad (3)$$

$$\frac{t}{q_t} = \frac{1}{k_2 q_e^2} + \frac{t}{q_e} \quad (4)$$

$$q_t = k_p t^{1/2} + C \quad (5)$$

k_1 (min^{-1}), k_2 (g·$mmol^{-1}$ min^{-1}) and kp represents the *pseudo*-first-order constant, second-order constant and intraparticle diffusion rate constant, respectively. C (mg g^{-1}) signifies the boundary layer effect. The kp and C were calculated from the plot qt vs $t^{0.5}$.

The adsorption isotherm data were concluded by fitting Langmuir (Equation 6), Freundlich (Equation 7), and Temkin (Equation 8) isotherm models:[41]

$$q_e = k_F \cdot C_e^{\frac{1}{n}} \quad (6)$$

$$q_e = \frac{q_m k_L c_e}{1 + k_L C_e} \quad (7)$$

$$q_e = \left(RT/_b\right) ln(ACe) \quad (8)$$

Where q_m (mg g^{-1}) represent fitted adsorption, K_L and k_F (mg L^{-1}) were the equilibrium adsorption constants of Langmuir and Freundlich respectively, n is the constant of heterogeneity and related to the intensity of adsorption. A (L g^{-1}) relates to the Temkin isotherm constant, b (KJ mol^{-1}) represents the Temkin constant relevant to the heat of

adsorption; T (K) is the absolute temperature and R (8.314 $\times 10^{-3}$ KJ/ mol K) is the general gas constant.

Disinfection assay: The minimal inhibitory concentration (MIC) assay was performed using standard broth microdilution technique [42]. In details, the bacterial strains were cultured to the mid-log growth phase in MHB medium and measured the absorbance at 600 nm equivalent to approximately 10^8 CFU mL^{-1}. Then, triplicate tenfold serial dilutions with culture medium were performed to obtain an inoculum of 10^5 CFU mL^{-1}. The PHMG~g~$MMCN_{@2.5}$ (16 mg mL^{-1}) were serial half-diluted to 10^{th} row in a 96-well plate. After inoculation of bacteria for 16 h at 37°C, the lowest concentration of PHMG~g~$MMCN_{@2.5}$ that inhibits visible growth of the bacteria was observed with the unaided eye and defined as MIC. The antimicrobial efficiencies of $MMCN_{@2.5}$, PHMB and PHMG~g~$MMCN_{@2.5}$ were systematically evaluated under series of concentrations of 0 μg mL^{-1} to 6.0 μg mL^{-1}, mixed with ~10^7 CFU mL^{-1} inoculum and incubated for 4 h at 37°C. Later, 100 μL mixtures were taken from each well and spread evenly on the LB agar plates in triplicate. Afterwards, the plates were incubated for overnight at 37°C to determine the number of survival colonies. For disinfections recycle performance evaluations, the collated PHMG~g~$MMCN_{@2.5}$ was washed several times with milli Q water to remove surface adhere dead bacterial strains and further added to fresh bacteria supernatant without any treatment to initiate the cyclic disinfection assay. The killing ratio was calculated according to equation (Equation 9):

$$\%\ \text{killing ratio} = \left(1-\frac{\text{cell count of control}}{\text{survivor count in mixture}}\right) \times 100\% \quad (9)$$

Simultaneous water purification assay of deionized and lake water matrices: The simultaneous adsorption of Tl(I) and disinfection of *S. aureus* and *E. coli* by

PHMG~g~MMCN$_{@2.5}$ were examined from pollutant spiked deionized and local Qixiang lake water, located in Shaanxi Province of China (34°1′30″–34°1′40″N, 108°45′30″–108°45′40″E) to simulate real time application scenario (important parameters of lake water are illustrated in Table S1, Supporting Information). To be effective, water samples were disinfected inside autoclave at 121°C for 20 min. In the set of experiments, 2 mg of nano-adsorbent were suspended in 20 mL volume containing 5 mg L^{-1} of Tl(I) metal and ~10^6 CFU mL^{-1} cultured *S. aureus* and *E. coli* strains. The solution was shaken for 4 h at 25 °C and PHMG~g~MMCN$_{@2.5}$ was separated by magnet. The 100 µL collected from solution supernatant were spread on Luria broth (LB) and further incubated overnight at 37 °C to determine the visible survival colonies of the bacteria. The results were calculated and analyzed according to equation 9. Another 5 mL sample were taken and filtered by 0.45 µm filter using polypyrene syringe and residual Tl(I) concentration was determined by ICP-OES analysis.

Supporting Information

Supporting Information is available from the Wiley Online Library.

Acknowledgment

This research was funded by National Natural Science Foundation of China (52073230), Ningbo Natural Science Foundation (202003N4006), the Joint Research Funds of Department of Science & Technology of Shaanxi Province, Northwestern Polytechnical University (2020GXLH-Z-013, 2020GXLH-Z-017).

Conflict of Interest

The authors declare no conflict of interest.

References

[1] S. Bolisetty, M. Peydayesh, R. Mezzenga, *Chem. Soc. Rev.* **2019**, 48, 463.

[2] Z. Zhao, Y. Xiong, X. Cheng, X. Hou, Y. Yang, Y. Tian, J. You, L. Xu, *J. Hazard. Mater.* **2020**, 393, 122378.
[3] R. J. Waldman, E. D. Mintz, H. E. Papowitz, *New. Eng. J. Med.* **2013**, 368, 592.
[4] W. W. Li, H. Q. Yu, Z. He, *Energ. Environ. Sci.* **2014**, 7, 911.
[5] A. D. Shah, W. A. Mitch, *Environ. Sci. Technol.* **2012**, 46, 119.
[6] J. Wang, J. Lu, Y. Zhou, Y. Zhou, *ACS ES&T Water* **2021**, 1, 479.
[7] R. Das, C. D. Vecitis, A. Schulze, B. Cao, A. F. Ismail, X. Lu, J. Chen, S. Ramakrishna, *Chem. Soc. Rev.* **2017**, 46, 6946.
[8] a) M. Zhang, X. Xie, M. Tang, C. S. Criddle, Y. Cui, S. X. Wang, *Nat. commun.* **2013**, 4, 1866; b) S. J. Tesh, T. B. Scott, *Adv. Mater.* **2014**, 26, 6056; c) X. Zhang, J. Qian, B. Pan, *Environ. Sci. Technol.* **2016**, 50, 881.
[9] a) B. Ramalingam, M. M. R. Khan, B. Mondal, A. B. Mandal, S. K. Das, *ACS. Sustain. Chem. Eng.* **2015**, 3, 2291; b) W. Che, Z. Xiao, Z. Wang, J. Li, H. Wang, Y. Wang, Y. Xie, *ACS. Sustain. Chem. Eng.* **2019**, 7, 5134; c) N. Mohammed, N. Grishkewich, K. C. Tam, *Environ. Sci. Nano.* **2018**, 5, 623.
[10] a) H. Su, Q. Tian, C.-A. Hurd Price, L. Xu, K. Qian, J. Liu, *Nano Today* **2020**, 31, 100834; b) L. Peng, H. Peng, C. T. Hung, D. Guo, L. Duan, B. Ma, L. Liu, W. Li, D. Zhao, *Chem* **2021**, 7, 1020; c) B. Qiu, L. Xie, J. Zeng, T. Liu, M. Yan, S. Zhou, Q. Liang, J. Tang, K. Liang, B. Kong, *Adv. Funct. Mater.* **2021**, 31, 2010694; d) Y. Zhang, Q. Yue, L. Yu, X. Yang, X. F. Hou, D. Zhao, X. Cheng, Y. Deng, *Adv. Mater.* **2018**, 30, 1800345; e) Q. Yue, Y. Zhang, Y. Jiang, J. Li, H. Zhang, C. Yu, A. A. Elzatahry, A. Alghamdi, Y. Deng, D. Zhao, *J. Am. Chem. Soc.* **2017**, 139, 4954.
[11] a) L. Duan, C. Wang, W. Zhang, B. Ma, Y. Deng, W. Li, D. Zhao, *Chem. Rev.* **2021**, DOI: 10.1021/acs.chemrev.1c00236; b) A. Saleem, Y. Zhang, M. Usman, M. Haris, P. Li, *Nano Today* **2022**, 46, 101607.
[12] Z. Wang, H.-C. Yang, F. He, S. Peng, Y. Li, L. Shao, S. B. Darling, *Matter* **2019**, 1, 115.
[13] L. Yu, K. Li, J. Zhang, H. Jin, A. Saleem, Q. Song, Q. Jia, P. Li, *ACS. App. Bio. Mater.* **2022**, DOI: 10.1021/acsabm.1c01132.

[14] a) X. Yang, P. Lu, L. Yu, P. Pan, A. A. Elzatahry, A. Alghamdi, W. Luo, X. Cheng, Y. Deng, *Adv Funct. Mater.* **2020**, 30, 2002488; b) L. Peng, C. T. Hung, S. Wang, X. Zhang, X. Zhu, Z. Zhao, C. Wang, Y. Tang, W. Li, D. Zhao, *J. Am. Chem. Soc.* **2019**, 141, 7073.

[15] J. Tang, J. Liu, C. Li, Y. Li, M. O. Tade, S. Dai, Y. Yamauchi, *Angew. Chem. Int. Ed.* **2015**, 54, 588.

[16] a) Y. Gao, S. Zhao, Z. Qiao, Y. Zhou, B. Song, Z. Wang, J. Wang, *Desalination* **2018**, 430, 74; b) Y. Gao, L. Liang, S. Zhao, Y. Qi, W. Zhang, X. Sun, Z. Wang, J. Wang, B. Song, *RSC. Adv.* **2018**, 8, 24690; c) Y. Tian, Y. Cao, Y. Wang, W. Yang, J. Feng, *Adv.Mater*. **2013**, 25, 2980.

[17] F. Xu, Z. Tang, S. Huang, L. Chen, Y. Liang, W. Mai, H. Zhong, R. Fu, D. Wu, *Nat. commun.* **2015**, 6, 7221.

[18] Z. Zhao, L. Duan, Y. Zhao, L. Wang, J. Zhang, F. Bu, Z. Sun, T. Zhang, M. Liu, H. Chen, Y. Yang, K. Lan, Z. Lv, L. Zu, P. Zhang, R. Che, Y. Tang, D. Chao, W. Li, D. Zhao, *J. Am. Chem. Soc.* **2022**, 144, 11767.

[19] Q. Yue, M. Wang, Z. Sun, C. Wang, C. Wang, Y. Deng, D. Zhao, *J. Mater. Chem. B.* **2013**, 1, 6085.

[20] H. Ma, J. Wang, Y. Su, N. Li, A. Saleem, J. Fan, W. Tian, P. Li, *ACS. App. Polym. Mater.* **2022**, 4, 1576.

[21] X. He, L. Dai, L. Ye, X. Sun, O. Enoch, R. Hu, X. Zan, F. Lin, J. Shen, *Adv. Sci.* **2022**, 9, 2105223.

[22] W. Peng, H. Yin, P. Liu, J. Peng, J. Sun, X. Zhang, Y. Gu, X. Dong, Z. Ma, J. Shen, P. Liu, *Chem. Eng. J.* **2021**, 412, 128707.

[23] W. Plazinski, W. Rudzinski, A. Plazinska, *Adv. Colloid. Interf. Sci.* **2009**, 152, 2.

[24] M. Haris, M. Usman, F. Su, W. Lei, A. Saleem, Y. Hamid, J. Guo, Y. Li, *Chem. Eng. J.* **2022**, 434, 134842.

[25] J. Liu, S. Ren, J. Cao, D. C. W. Tsang, J. Beiyuan, Y. Peng, F. Fang, J. She, M. Yin, N. Shen, J. Wang, *J. Hazard. Mater.* **2021**, 401, 123311.

[26] Q. Zhao, M. Seredych, E. Precetti, C. E. Shuck, M. Harhay, R. Pang, C. X. Shan, Y. Gogotsi, *ACS Nano* **2020**, 14, 11787.

[27] K. Fu, X. Liu, C. Lv, J. Luo, M. Sun, S. Luo, J. C. Crittenden, *Environ. Sci. Technol.* **2022**, 56, 2677.
[28] A. Saleem, J. Wang, T. Sun, F. Sharaf, M. Haris, S. Lei, *J. Environ. Chem. Eng.* **2020**, 8, 104430.
[29] H. Xu, Y. Luo, P. Wang, J. Zhu, Z. Yang, Z. Liu, *Water. Res.* **2019**, 165, 114981.
[30] B. Tansel, *Sep. Purif. Technol.* **2012**, 86, 119.
[31] a) J. Tang, W. Wu, L. Yu, X. Fan, G. Liu, Y. Yu, *Sci. Total. Environ.* **2019**, 694, 133625; b) G. Zhang, F. Fan, X. Li, J. Qi, Y. Chen, *Chem. Eng. J.* **2018**, 331, 471.
[32] J. Liu, W. Chen, X. Hu, H. Wang, Y. Zou, Q. He, J. Ma, C. Liu, Y. Chen, X. Huangfu, *Chem. Eng. J.* **2021**, 416, 127919.
[33] a) Y. Jiang, R. Raliya, P. Liao, P. Biswas, J. D. Fortner, *Environ. Sci. Nano.* **2017**, 4, 1484; b) W. L. Sun, J. Xia, S. Li, F. Sun, *Chem. Eng. J.* **2012**, 200-202, 627.
[34] T. K. Nissinen, I. T. Miettinen, P. J. Martikainen, T. Vartiainen, *Chemosphere* **2001**, 45, 865.
[35] M. Yin, Y. Zhou, D. C. W. Tsang, J. Beiyuan, L. Song, J. She, J. Wang, L. Zhu, F. Fang, L. Wang, J. Liu, Y. Liu, G. Song, D. Chen, T. Xiao, *J. Hazard. Mater.* **2021**, 407, 124402.
[36] a) A. Cano, L. Reguera, M. Avila, D. Velasco-Arias, E. Reguera, **2020**, 2020, 137; b) H. Zhang, J. Qi, F. Liu, Z. Wang, X. Ma, D. He, *J. Hazard. Mater.* **2022**, 423, 126972.
[37] S. Roy, S. Sarkhel, D. Bisht, S. N. Hanumantharao, S. Rao, A. Jaiswal, *Biomater. Sci.* **2022**, 10, 4392.
[38] J. Liu, Z. Sun, Y. Deng, Y. Zou, C. Li, X. Guo, L. Xiong, Y. Gao, F. Li, D. Zhao, *Angew. Chem. Int. Ed* **2009**, 48, 5875.
[39] W. Stöber, A. Fink, E. Bohn, *J. Colloid. Interf. Sci.* **1968**, 26, 62.
[40] J. Wang, X. Guo, *J. Hazard. Mater.* **2020**, 390, 122156.
[41] M. A. Al-Ghouti, D. A. Da'ana, *J. Hazard. Mater.* **2020**, 393, 122383.
[42] I. Wiegand, K. Hilpert, R. E. W. Hancock, *Nat. Prot.* **2008**, 3, 163.

A unique class of radially gradient mesoporous nano-adsorbent was designed through a micelle interface assembly approach with tempting antimicrobial moieties, which exhibit dual functionality of toxic thallium Tl(I) removal and high disinfection capability towards *S. aureus* and *E. coli* bacterial strains.

Atif Saleem [1], Jingjie Chen [1], Meng Liu [1], Nian Liu [1], Muhammad Usman [2], Ke Wang [1], Muhammad Haris [3], Yuezhou Zhang [1,4], Peng Li [1*]*

Micelle interface assembled duel functional Nano-adsorbent

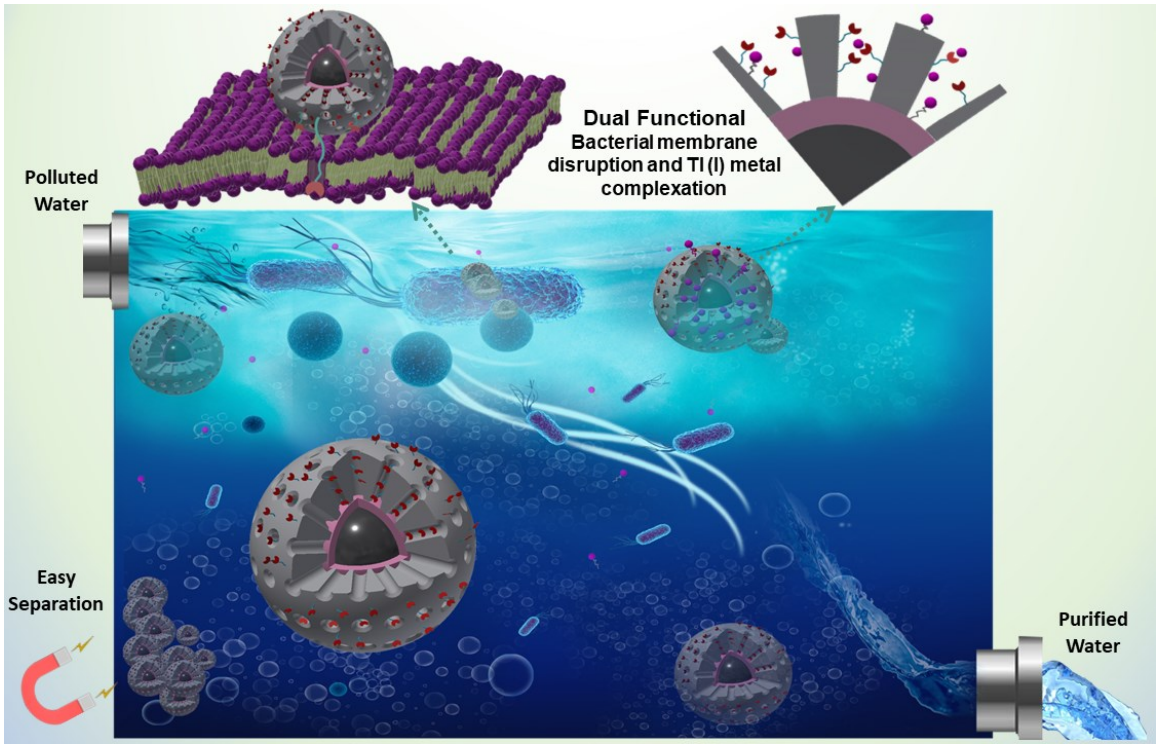

Supporting Information

Versatile Magnetic Mesoporous Carbon Derived Nano-adsorbent for Synchronized Toxic Metal Removal and Bacterial Disinfection from Water Matrices

Atif Saleem 1, Jingjie Chen 1, Meng Liu 1, Nian Liu 1, Muhammad Usman 2, Ke Wang 1, Muhammad Haris 3, Yuezhou Zhang 1,4, Peng Li 1**

Materials and characterization

Materials: $FeCl_3 \cdot 6H_2O$, trisodium citrate, sodium acetate, ethylene glycol, ethanol, NaOH, $NaHCO_3$, NaH_2PO_4, HCl, NH_4.OH (28 wt%), tetraethyl orthosilicate (TEOS), dopamine hydrochloride, Triblock poly(ethylene oxide)-b-poly(propylene oxide)-bpoly(ethylene oxide), (Pluronic F127, $PEO_{106}PPO_{70}PEO_{106}$, Mav = 12600), 1,3,5-trimethyl benzene (TMB), and Tetrahydrofuran (THF) (> 99%), were purchased from Sigma-Aldrich. *N,N*-dicyclohexyl-carbodiimide (DCC), *N,N*-dimethylformamide (DMF), and 4-dimethylaminopyridine (DMAP) were bought from J&K Scientific Ltd., China. Poly(hexamethylenebiguanide) hydrochloride (PHMB, 99%) was obtained from Wonda Science. Mueller Hinton broth (MHB) was purchased from Oxford, U.K. *S. aureus* (ATCC29213) and *E. coli* (ATCC8739) used were purchased from American Type Culture Collection (ATCC). All chemicals were used as received without any further purification. The Millipore water was used for all experiments.

Characterization: Transmission electron microscopy (TEM) was used to differentiate the morphological difference among tailored nanostructures. Scanning electron microscopy-energy dispersive spectroscopy (SEM-EDS) was deployed to define the elemental composition. Nitrogen adsorption-desorption isotherms was measured at 77 K with a

Micromeritics Tristar 3000 analyzer. The Brunauer-Emmett-Teller (BET) method was adopted to calculate the specific surface areas in a relative pressure range from 0.005 to 0.25. By using the Barrett-Joyner-Halenda (BJH) model, the pore volumes and pore size distributions was derived from the adsorption branches of isotherms, and the total pore volumes (Vt) was estimated from the adsorbed amount at a relative pressure P/P0 of 0.995. FTIR spectra was collected by using KBr wafers technique. The ζ-potential was monitored by DLS (Malvern ZetasizerNano ZS) in water solution at 25 °C. Raman spectrophotometer (LabRAM HR Evolution, Horiba Scientific, Germany) with a 532 nm laser (mpc3000) as excitation source was performed. The cationic polymers content was determined by Thermogravimetric analysis (TGA) NETZSCHSTA 409 TG-DTA (Germany). Magnetic saturation was analyzed with a magnetometer (Lake Shore 7404) at 25 °C. X-ray photoelectron spectroscopy (XPS) analysis was determined to investigate surface functionalization by using an Al Kα source (1486.6 eV of photons).

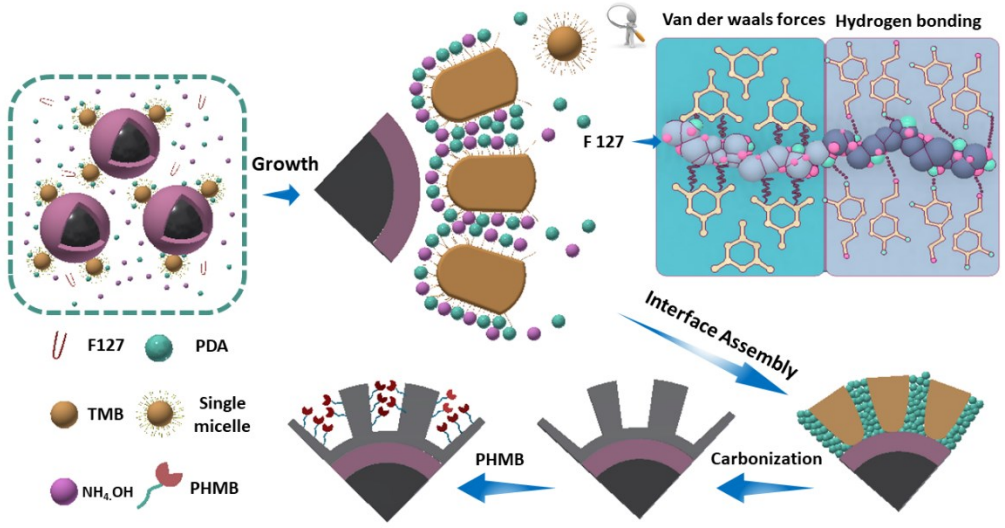

Figure S1. Preparation mechanism of the gradient magnetic mesoporous carbon nanosphere by the programmable emulsion induced interface assembly strategy and post

functionalization with antimicrobial PHMB polymer.

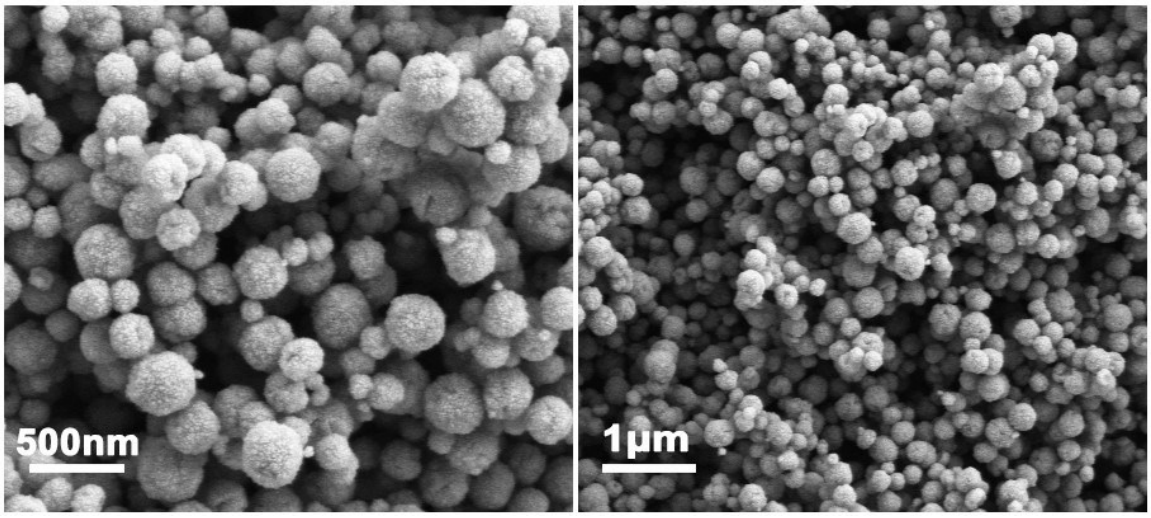

Figure S2. FESEM observations of uniform magnetic nanocore spheres.

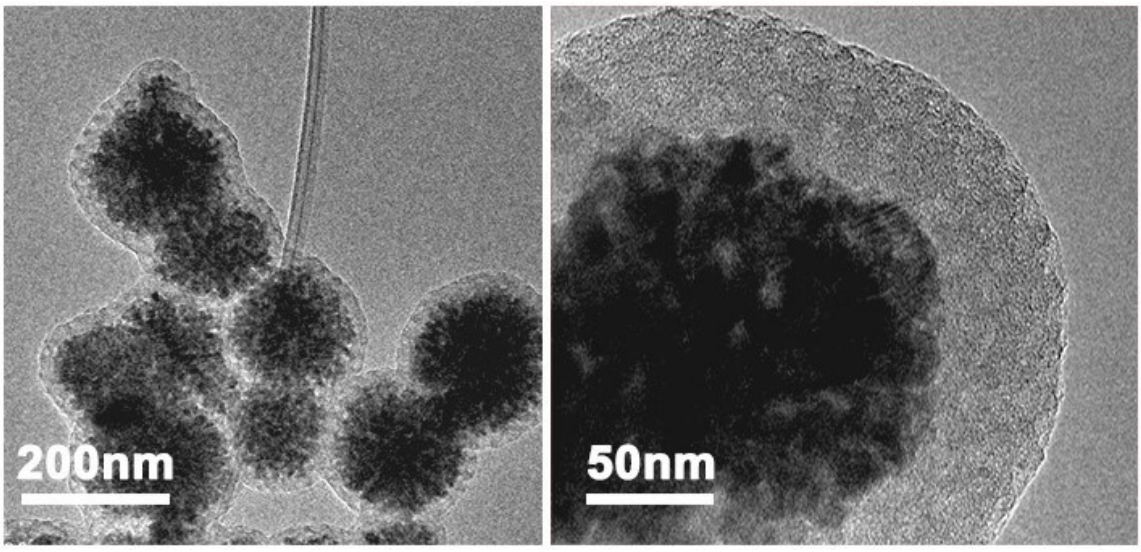

Figure S3. TEM observations of gradient mesoporous PHMB~g~MMCN$_{@2.5}$.

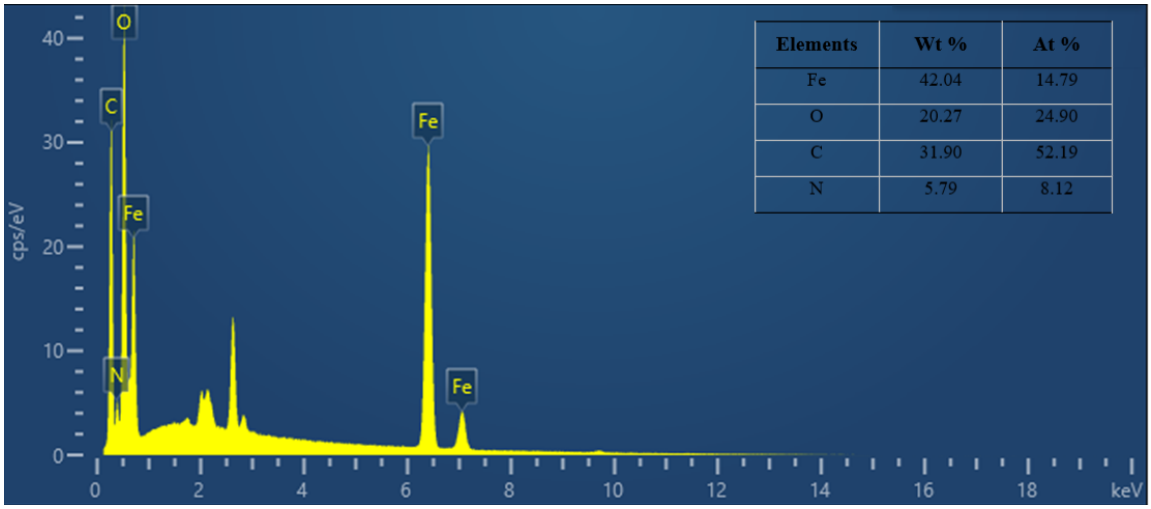

Elements	Wt %	At %
Fe	42.04	14.79
O	20.27	24.90
C	31.90	52.19
N	5.79	8.12

Figure S4. Energy dispersive X-ray (EDX) spectrum of element present in the PHMB~g~MMCN$_{@2.5}$ and inset quantitative table.

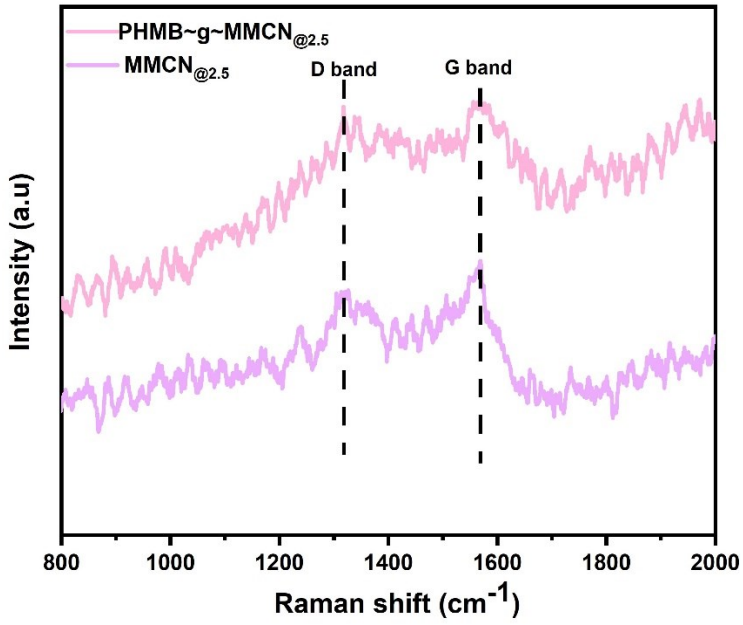

Figure S5. Raman spectrum of the gradient MMCN$_{@2.5}$, and PHMB~g~MMCN$_{@2.5}$.

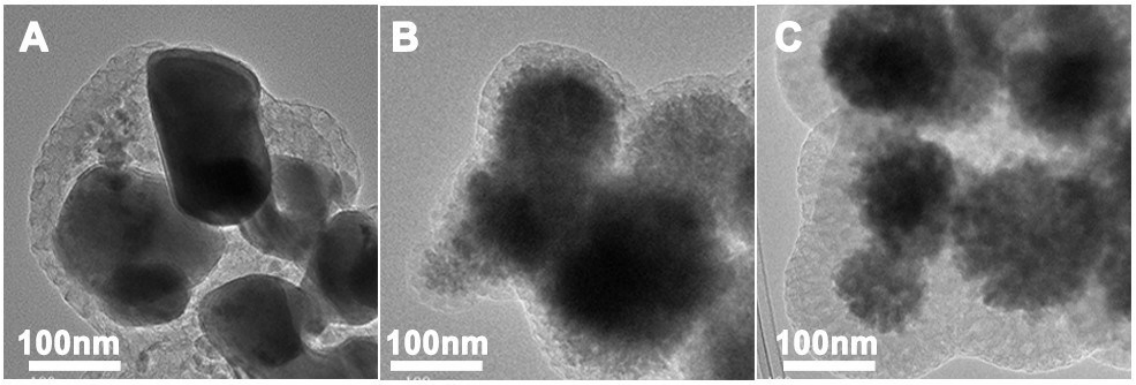

Figure S6. TEM observations of magnetic nanocores synthesis and interface deposition of PDA shell: (A) Pristine magnetic nanocore interface assembly of PDA shell, (B) Nonporous silica encapsulated magnetic nanocore interface assembly of PDA shell, (C) Gradient MMCN nanospheres fabricated by trisodium citrate modified nanocore smart interface co assembly of mesoporous PDA shell.

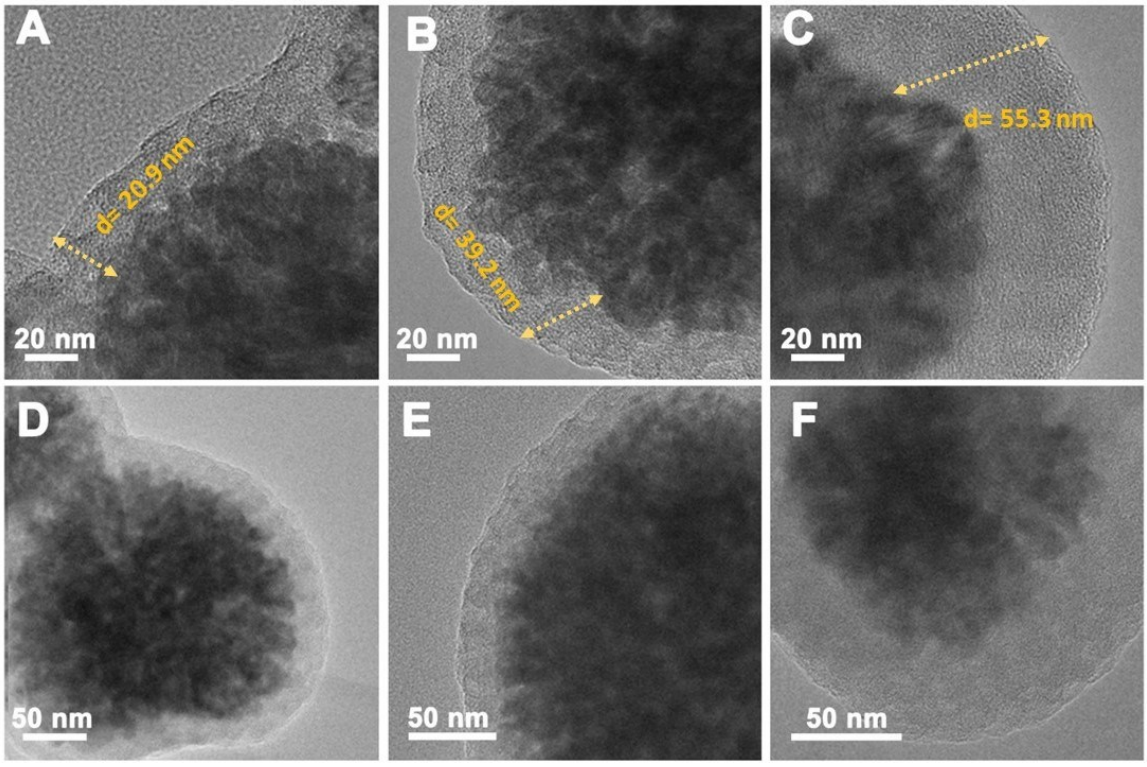

Figure S7. Magnified TEM images for observing structural and diameter evolution of the $MMCN_{@x}$ at different concentration of NH4.OH. The mesoporous carbon nanospheres prepared at (A-D) 1 mL, (B-E) 2.5 mL, (C-F) 5.0 mL.

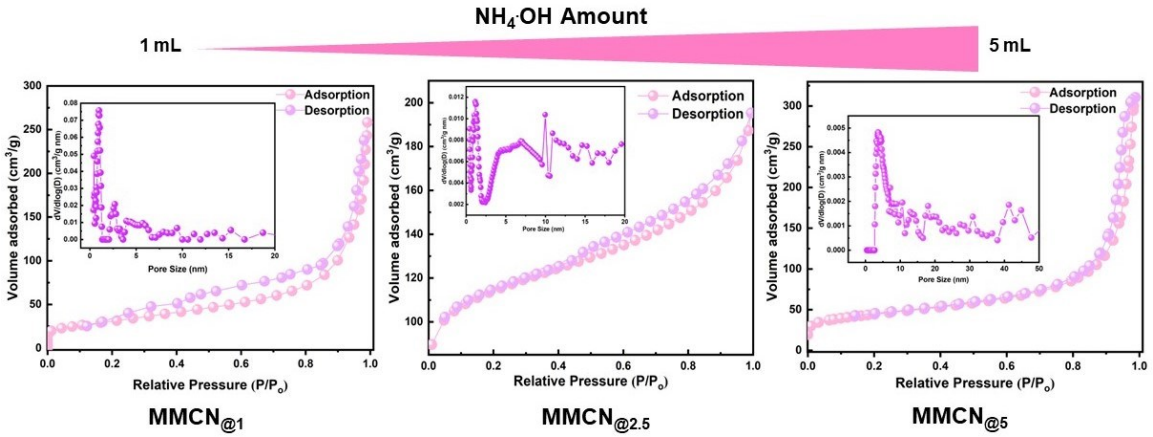

Figure S8. Surface area and inset pore size graphical illustration of magnetic mesoporous carbon synthesized at varying concentration of NH_4OH.

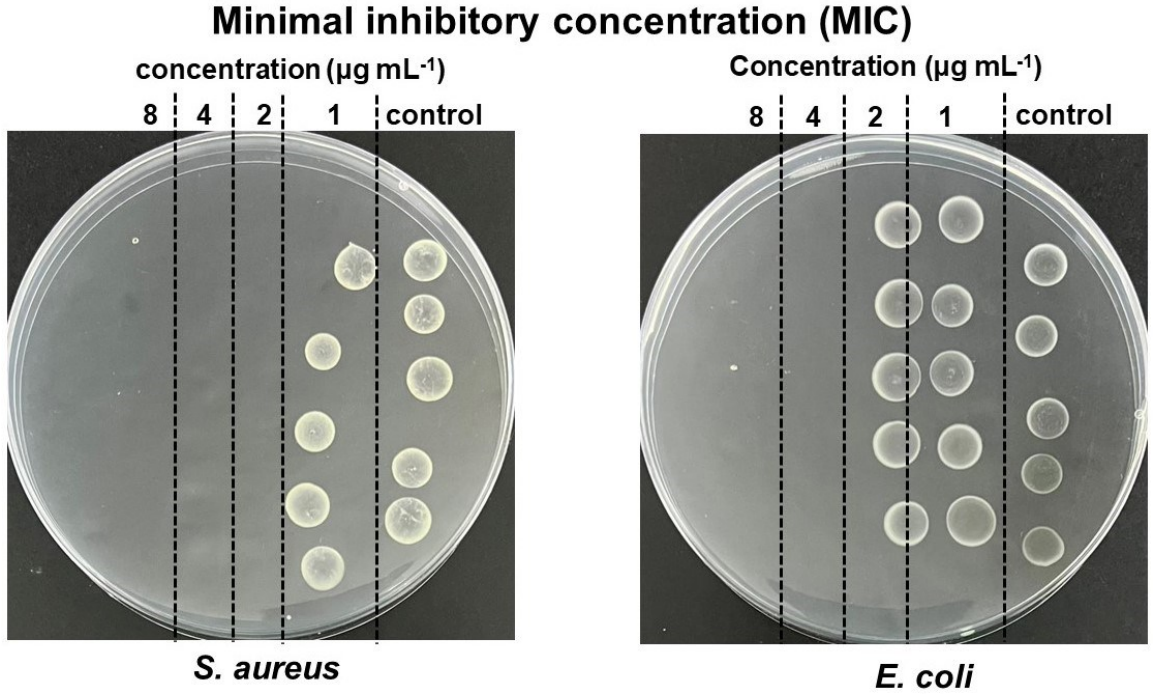

Figure S9. Optical images of MIC assay towards *S. aureus* and *E. coli* at varying concentration of PHMG~g~$MMCN_{@2.5}$.

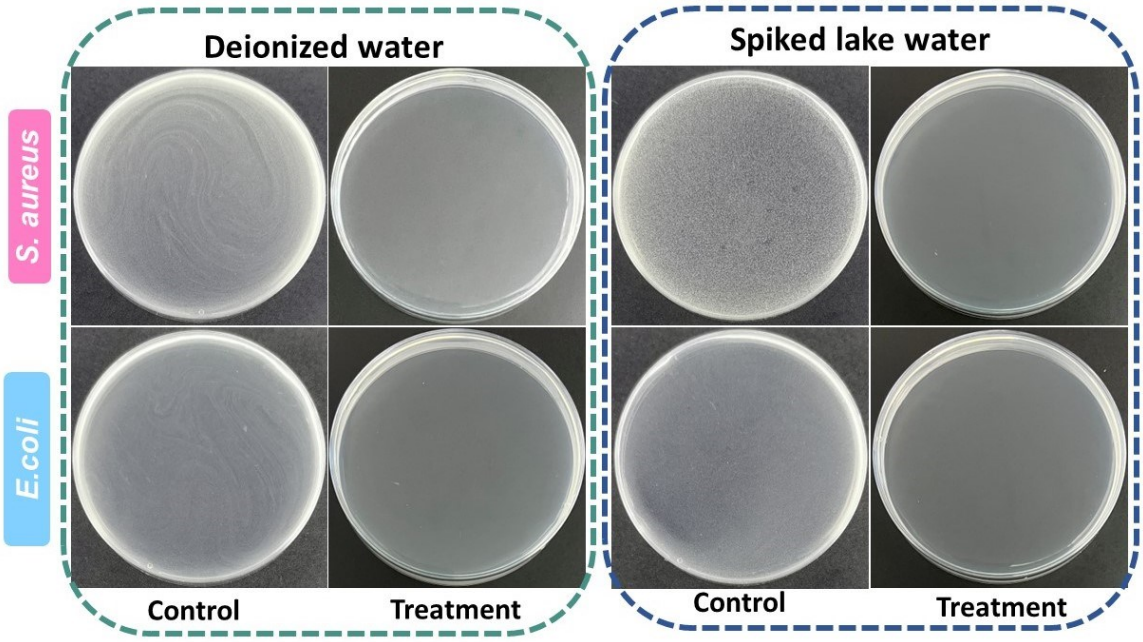

Figure S10. Bacterial colonies images cultured from deionized and lake water matrices before and after treatment to assay simultaneous real time water purification assay.

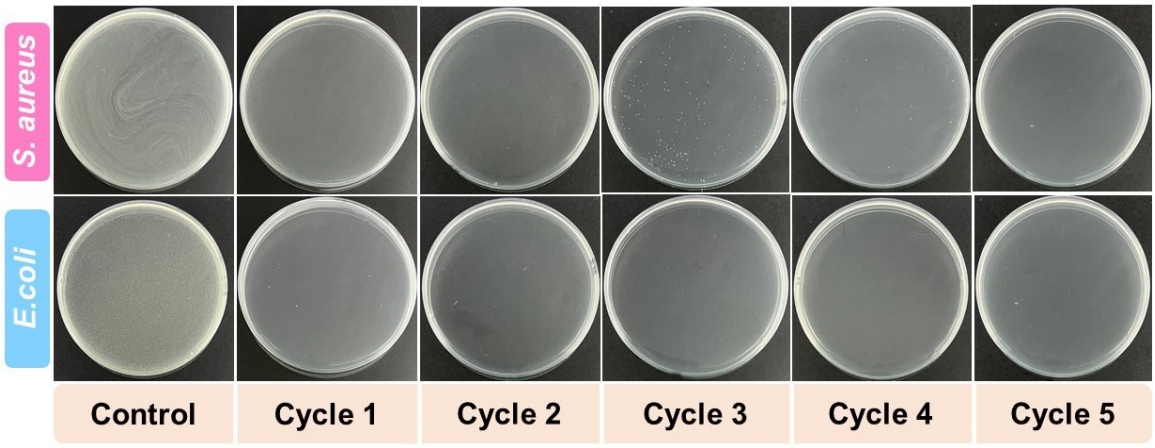

Figure S10. Disinfection performance optical images of PHMB~g~MMCN$_{@2.5}$ against cultured *S. aureus* and *E. coli* after five consecutive regeneration cycles.

Table S1. Basic parameters of sampled surface water (mean ± SD).

pH	DO (mg L^{-1})	Cond(μ s/cm)	TOC	T1(I) (mg. L^{-1})	TN	Ca(II) (mg. L^{-1})	Mg(II) (mg. L^{-1})	K((I) (mg. L^{-1})
8.01±0.02	6.24±0.1	347±5	10±1	0.0001	4.35±0.02	8.2±0.2	8.4±3	1.1±0.1

COD = Chemical oxygen demand; TOC = Total organic carbon; TN = Total nitrogen

Table S2. T1(I) removal performance of series of reported adsorbent.

Adsorbents	Dosage (g L^{-1})	Equilibrium Concentration (mg L^{-1})	Equilibrium time (h)	pH	Adsorption Capacity (mg g^{-1})	References
Saw dust	100	0-1000	24	7.0	13.2	[1]
Prussian blue alginate	1	0-400	72	4.0	103	[2]
MnO_2-FeOOH	0.5	0-400	24	7.0	236.4	[3]
Biochar nanosheets	0.1	0.250	24	7.0	382.38	[4]
MnO_2@pyrite	0.5	0-160	0.5	12.0	320.1	[5]
PAAm@Bentonite composite	10	0-1000	24	5.0	73.6	[6]
Sugar pulp	7	0-20,000	0.25	5.5	185.2	[6]
TNT	0.2	0-60	3	5.0	709.2	[7]
HMO	0.5	0-100	24	5.0	353.6	[8]
Fe_3O_4@PB	0.2	0-400	24	7.0	528	[9]
TiO_2	0.2	0-80	24	7.0	302.6	[10]
PHMB~g~$MMCN_{@2.5}$	0.02	0-350	24	7.0	559	Present study

Table S3. Ionic properties of interfering cations.

Cations	Hydration Energy kJ/mol	Ionic radius Å	Electronegativity	Hydrated ionic radius Å
K^+	-351	1.38	0.82	3.30
Na+	-435	0.11	0.93	7.16
Tl^+	-300	1.50	1.62	3.30
Ca^{2+}	-1306	0.99	1.00	4.12
Mg^{2+}	-1922	0.72	1.31	4.28
Cu^{2+}	-2160	0.73	1.90	4.19
Zn^{2+}	-2044	0.83	1.65	4.30

Hydration energy, Ionic radius, electronegativity and hydrated ionic radius reported from literature [11]

References

[1] S. Q. Memon, N. Memon, A. R. Solangi, J.-u.-R. Memon, *Chem. Eng. J.* **2008**, 140, 235.

[2] T. Vincent, J.-M. Taulemesse, A. Dauvergne, T. Chanut, F. Testa, E. Guibal, *Carbohyd. Polym.* **2014**, 99, 517.

[3] M. Chen, P. Wu, L. Yu, S. Liu, B. Ruan, H. Hu, N. Zhu, Z. Lin, *J.Environ. Manag.* **2017**, 192, 31.

[4] M. Haris, M. Usman, F. Su, W. Lei, A. Saleem, Y. Hamid, J. Guo, Y. Li, *Chem. Eng. J.* **2022**, 434, 134842.

[5] H. Li, X. Li, T. Xiao, Y. Chen, J. Long, G. Zhang, P. Zhang, C. Li, L. Zhuang, K. Li, *Chem.Eng. J.* **2018**, 353, 867.

[6] Z. M. Şenol, U. Ulusoy, *Chem. E. J.* **2010**, 162, 97.

[7] W. Liu, P. Zhang, A. G. L. Borthwick, H. Chen, J. Ni, *J.Colloid. Interf. Sci.* **2014**, 423, 67.

[8] S. Wan, M. Ma, L. Lv, L. Qian, S. Xu, Y. Xue, Z. Ma, *Chem. Eng. J.* **2014**, 239, 200.

[9] H. Zhang, J. Qi, F. Liu, Z. Wang, X. Ma, D. He, *J.Hazard. Mater.* **2022**, 423, 126972.

[10] G. Zhang, J. Luo, H. Cao, S. Hu, H. Li, Z. Wu, Y. Xie, X. Li, *Sci. Rep.* **2022**, 12, 72.

[11] a) T. B. Kinraide, U. Yermiyahu, *J.Inorg. Biochem.* **2007**, 101, 1201; b) B. Tansel, *Sep.Purif. Technol.* **2012**, 86, 119.